

THE T16 PROJECT: IMAGE SUBTRACTION LIGHT CURVES FROM TESS CYCLE 1 FULL-FRAME  
IMAGES FOR STARS WITH  $T < 16$

JOEL D. HARTMAN,<sup>1</sup> GÁSPÁR Á. BAKOS,<sup>1,2,\*</sup> LUKE G. BOUMA,<sup>3,4</sup> AND ZOLTAN CSUBRY<sup>1</sup>

<sup>1</sup>*Department of Astrophysical Sciences, Princeton University, NJ 08544, USA*

<sup>2</sup>*MTA Distinguished Guest Fellow, Konkoly Observatory, Hungary*

<sup>3</sup>*Observatories of the Carnegie Institution for Science, 813 Santa Barbara Street, Pasadena, CA 91101, USA*

<sup>4</sup>*Department of Astronomy, California Institute of Technology, Pasadena, CA 91125, USA*

ABSTRACT

We present 83,717,159 light curves for 56,401,549 stars with  $T < 16$  mag observed in the Full-Frame Images (FFIs) of Cycle 1 of the NASA *TESS* mission. These light curves were extracted from subtracted images produced by the Cluster Difference Imaging Survey (CDIPS; Bouma et al. 2019). We make public the raw image subtraction light curves, together with light curves de-trended against instrumental systematics. We compare the light curves to other publicly available light curves from the *TESS* FFIs, finding that for a substantial fraction of stars with  $T < 16$ , the T16 project provides the highest precision FFI light curves available. We demonstrate that the detrended T16 light curves are generally as good as, or better than, than the light curves from other projects for the known TOIs. We also show that the un-detrended light curves can be used to study high amplitude variable stars. The light curves are being made available through the NASA Mikulski Archive for Space Telescopes (MAST). Light curve production is underway for additional *TESS* Cycles.

*Keywords:* light curves, photometry

Corresponding author: Joel Hartman  
[jhartman@astro.princeton.edu](mailto:jhartman@astro.princeton.edu)

\* Packard Fellow

## 1. INTRODUCTION

The NASA *Transiting Exoplanet Survey Satellite* (*TESS*; Ricker et al. 2015) mission has conducted an unprecedented, nearly all-sky, space-based survey for small transiting planets around bright stars. During the primary mission approximately 307,000 stars with  $T \lesssim 12$  mag were observed every two minutes at high photometric precision for a duration of  $\sim 1$  month near the ecliptic plane, and up to 1 year of continuous observations near the ecliptic poles. Light curves for these stars were produced by the *TESS* Science Processing Operations Center (SPOC; Jenkins et al. 2016) at NASA Ames and have been searched for transit signals and made publicly available on the NASA Mikulski Archive for Space Telescopes (MAST).

*TESS* has been approved for two extended missions so far. During the first two year extended mission (from 2020 July through 2022 September) the Southern ecliptic hemisphere was re-observed, while the pointings for the Northern ecliptic hemisphere observations were adjusted to include a set of observations along the ecliptic plane, and a set of observations concentrated on the ecliptic pole. During the ongoing second extended mission *TESS* is observing fields both in the Northern and Southern ecliptic hemispheres.

In addition to the 2 minute cadence targets, stacked full-frame images (FFIs) were downloaded from the spacecraft. These were obtained at a cadence of 30 minutes, 10 minutes, and 200 seconds for the primary mission, first extended mission, and second extended mission, respectively. Included in the *TESS* FFIs are more than 100 million stars with  $T < 16$  mag for which *TESS* should produce light curves with a 1 hr photometric precision better than 1%.

At the time of writing, there are seven efforts, besides that presented here, that have released large collections of *TESS* FFI light curves as High Level Science Products (HLSPs) on MAST. These are summarized in Table 1.

The two projects that have covered the most sectors to date are the MIT Quick-Look Pipeline (QLP; Huang et al. 2020a) project, and the *TESS* Science Processing Operations Center Full Frame Image (*TESS*-SPOC FFI, hereafter *TESS*-SPOC; Caldwell et al. 2020) project at NASA Ames. The former has released light curves for all stars with  $T < 13.5$ , the latter has released light curves for a more selected sample of up to 160,000 stars per sector. The *TESS*-SPOC targets have either  $H < 10$  mag, or  $T < 13.5$  mag, or a distance within 100 pc. Both of these pipelines utilize aperture photometry to extract the photometric measurements, followed by post-processing of the light curves to correct for instrumental systematic variations in the measurements.

Two other efforts to produce light curves for all stars down to  $T < 16$  include the *TESS Gaia* Light Curve project (TGLC; Han & Brandt 2023), and the Goddard Space Flight Center *eleanor lite* project (GSFC-ELEANOR-LITE, hereafter GSFC; Powell et al. 2022). The former uses aperture and PSF-fitting photometry, and utilizes the *Gaia* catalog (Gaia Collaboration et al. 2018) to correct for flux from neighboring stars, while the GSFC project uses “simple aperture” photometry through the *eleanor* tool (Feinstein et al. 2019) to produce light curves. Both of these projects have released light curves for the first two *TESS* Cycles, while TGLC has released light curves for the third *TESS* Cycle as well. Both projects greatly exceed QLP and *TESS*-SPOC in terms of the total number of light curves made public.

Finally three projects have published light curves for particular classes of stars. This includes the DIAMANTE project (Montalto et al. 2020; Montalto 2023), which uses the image subtraction method of photometry (e.g., Alard & Lupton 1998), and has made light curves public for transiting planet candidates, and the PATHOS (Nardiello et al. 2019, 2020; Nardiello 2020; Nardiello et al. 2021) and Cluster Difference Imaging Photometric Survey (CDIPS; Bouma et al. 2019) projects which use PSF photometry, and image subtraction photometry, respectively, and have made public light curves for young stars and stars that are members of clusters.

In this paper, we build on the prior work of the CDIPS project to release image-subtraction-derived light curves for *all* stars with  $T < 16$  mag in the *TESS* Cycle 1 FFI observations.

In the following section we briefly describe the *TESS* observations. In Section 3 we discuss the methods used to produce the T16 light curves. We describe the resulting dataset, its precision, and a comparison to other sets of light curves in Section 4. We conclude the paper in Section 5.

## 2. TESS OBSERVATIONS

Here we present light curves from the first year of *TESS* observations, dubbed Cycle I. This cycle was divided into 13 observing campaigns, called sectors. Each sector consisted of two consecutive 13.7 day elliptical orbits of the *TESS* spacecraft. Every perigee the spacecraft paused observations for approximately 3 hr to downlink the data to Earth. Momentum dumps, where the speed of the spacecraft momentum wheels were reset, were performed every 2.5 days. The pointing of the spacecraft is destabilized at these periods, causing sys-

**Table 1.** Summary of projects that have released FFI light curves as HLSPs on MAST

| Project Name      | Sectors <sup>a</sup><br>Covered | Target<br>Selection                               | Photometric<br>Method       | Number of<br>Stars | Number of<br>Light Curves | References         |
|-------------------|---------------------------------|---|-----------------------------|--------------------|---------------------------|--------------------|
| TGLC              | 1–41                            | $T < 16$  | Aperture and PSF Photometry | $9.4 \times 10^7$  | $2.4 \times 10^8$         | (13)               |
| GSFC-ELEANOR-LITE | 1–26                            | $T < 16$  | Aperture Photometry         | $9.3 \times 10^7$  | $1.5 \times 10^8$         | (14)               |
| QLP               | 1–80                            | $T < 13.5$  | Simple Aperture Photometry  | $2.0 \times 10^7$  | $7.5 \times 10^7$         | (1) (2) (3) (4)    |
| TESS-SPOC         | 1–72                            | $N_{\text{targets}} < 1.6 \times 10^5$ per sector | Simple Aperture Photometry  | $3.8 \times 10^6$  | $1.1 \times 10^7$         | (5)                |
| CDIPS             | 1–55                            | Star cluster members or young stars               | Image Subtraction           | $1.2 \times 10^6$  | $2.4 \times 10^6$         | (6)                |
| PATHOS            | 1–26                            | Star cluster members                              | PSF Photometry              | $2.7 \times 10^5$  | $3.9 \times 10^5$         | (9) (10) (11) (12) |
| DIAMANTE          | 1–26                            | Transiting Planet Candidates                      | Image Subtraction           | 1556               | 1556                      | (7) (8)            |
| T16               | 1–13                            | $T < 16$  | Image Subtraction           | $5.6 \times 10^7$  | $8.4 \times 10^7$         | this work          |

**References**—(1) Huang et al. (2020a); (2) Huang et al. (2020b); (3) Kunimoto et al. (2021); (4) Kunimoto et al. (2022); (5) Caldwell et al. (2020); (6) Bouma et al. (2019); (7) Montalto et al. (2020); (8) Montalto (2023); (9) Nardiello et al. (2019); (10) Nardiello et al. (2020); (11) Nardiello (2020); (12) Nardiello et al. (2021); (13) Han & Brandt (2023); (14) Powell et al. (2022);

<sup>a</sup> As of 2024 Dec 2.

tematic variations in the light curves that are associated with these events.

The *TESS* spacecraft uses four identical  $f/1.4$  lenses of pupil diameter 10.5 cm, and a field of view of  $24^\circ \times 24^\circ$ . The lenses are aligned so that the full *TESS* field of view is a  $24^\circ \times 96^\circ$  stripe on the sky. Each lens images onto a set of four  $2048 \times 2048$  back-illuminated MIT/Lincoln Laboratory CCID-80 detectors at a pixel scale of  $21'' \text{ pixel}^{-1}$ . The effective bandpass of the *TESS* instrument spans from 600 nm to 1000 nm, and is referred to as the  $T$ -band. The CCDs are read out at a cadence of 2 sec. In order to mitigate against cosmic rays, ten consecutive exposures are collected for each pixel, the brightest and faintest exposures in the collection are rejected, and the remaining eight pixels are summed. This procedure is repeated 90 times, co-adding the results, to produce the FFIs with an effective cadence of 30 min and exposure time of 24 min.

Altogether there are 16 different detectors used for a single *TESS* sector, and we reduce the observations from each sector and detector independently.

### 3. DATA REDUCTION METHODS

#### 3.1. Difference Image Photometry

We make use of the difference image reduction of the *TESS* FFIs carried out by the CDIPS project, and published in Bouma et al. (2019). Here we provide a brief summary of the reduction process, referring the reader to this prior work for details. We follow this summary with a more detailed description of the methods used to carry out the photometric measurements from the difference images that form the new contribution of the present work.

The CDIPS processing began with the calibrated *TESS* FFIs summarized in Section 2. An estimate of the large-scale background is first subtracted from the images, where the estimate is based on a median box-fitter followed by a Gaussian blurring. Saturated and other problematic pixels are masked and the WCS solutions included in the FFI headers, obtained from MAST, are verified for each image to exclude images with problematic astrometry. An astrometric reference image is then selected from the set of observations for a given combination of sector/camera/CCD. The background-subtracted science images are registered to the reference image using the existing WCS solutions and the tools within the FITSH package (Pál 2012). A photometric reference image is then produced for the sector/camera/CCD by aligning and matching the flux, background and PSF of a selection of  $\sim 50$  science frames using the FITSH tools. The reference image is then convolved to each science frame using the FICONV tool from the FITSH package, and the resulting difference images are the starting point for the new work that we describe in the present paper.

We then followed the process of Bouma et al. (2019) for the photometry, but here we made use of a much larger list of stars. Whereas the CDIPS project focused on making light curves for stars identified as potential members of open clusters, moving groups, stellar associations, or that were identified as candidate young stars, here we make light curves for all stars with  $T < 16$  mag in the Gaia DR2 catalog. We estimate  $T$  for each source from the *Gaia* DR2 photometry using eq. 1 from Stassun

et al. (2019):

$$\begin{aligned}
 T = G & \\
 & -0.00522555(BP - RP)^3 \\
 & +0.0891337(BP - RP)^2 \\
 & -0.633923(BP - RP) \\
 & +0.0324473,
 \end{aligned}
 \tag{1}$$

where  $BP$ ,  $RP$  and  $G$  are the magnitudes from the three different pass-bands in the *Gaia* catalog, and where we assume  $BP - RP = 0$  for sources where either measurement is unavailable.

We measure aperture photometry on the difference images using the WCS solutions and the fixed astrometric positions from *Gaia* to center the aperture for each source. Here we use the same set of three apertures as used by the CDIPS project, namely circular apertures of radii 1.0, 1.5 and 2.25 pixels. Differential flux photometry is measured using the FIPHOT program, included in FITSH. This process also subtracts from each measurement of the differential flux any residual positive or negative background on the difference images that are estimated using annuli of inner radius 7.0 pixels and outer radius 13 pixels.

To convert the differential flux measurements to total flux measurements we provide as input to FIPHOT an estimate of the flux on the photometric reference image of each source through each of the three apertures. Because stars on the reference image may be highly blended, rather than directly measuring this flux for each source, we make use of the  $G$ ,  $BP$  and  $RP$  photometry in the *Gaia* DR2 catalog. We determine a transformation from these magnitudes to fluxes on the photometric reference images through each of the apertures by fitting a relation to the observations for a set of uncrowded stars. We find that the scatter on this relation is typically  $\sim 0.1$  mag. Any errors in this process for an individual star will lead to an overall error on the amplitude of any variations in the resulting light curve, but will otherwise not affect the shape of the light curve or the signal-to-noise ratio of any variations that are present. Special caution should be taken for high amplitude variable stars, where the actual flux on the reference image may differ significantly from the expected flux based on the *Gaia* catalog photometry. This can lead to significant errors in the amplitude of variability in the derived light curves for these stars.

Note that any non-varying flux is automatically excluded from the difference images. Because we use the *Gaia* catalog photometry to determine the reference flux of each source, the resulting light curves that we produce will exclude any non-variable contamination from

blended neighbors. The resulting light curve is effectively corrected for dilution from any sources that are unresolved by *TESS*, but resolved by *Gaia*. However, if any star has an unresolved neighbor that is itself a variable, the variable flux from that neighbor may be sampled by the aperture used to measure the differential flux of the target star in question. The varying flux from the variable neighbor will then be combined with the estimated reference flux of the target star based on *Gaia* to produce a magnitude light curve that includes a contaminated variable signal. The amplitude of this signal, in magnitudes, can be exceedingly large in the case of a faint star that is blended with a bright variable star. In fact negative net fluxes, yielding NaN values for the magnitude, are possible if the differential flux from the variable neighbor is negative and has an absolute value that exceeds the estimated reference flux of the target star.

### 3.2. Light Curve Time Stamps

The *TESS* FFIs contain in the image headers the *TESS* Barycentric Julian Dates (TBJD) at the beginning and end of each observation. These are given on the Barycentric Dynamical Time (TDB) system, which differs from the UTC system by a discrete value that increments whenever leap-seconds are held in the UTC system. The barycentric corrections are applied for the sky coordinates of a specified pixel in the image. Because each source observed in the image has a different sky position, separate barycentric corrections need to be applied for each light curve. To do this we first compute the mid BJD time for each observation from the image headers, and subtract the applied barycentric correction to determine the JD at the time of observation. We then use the VARTOOLS program (Hartman & Bakos 2016) to convert the JD to BJD for each source. Here we use the *Gaia* DR3 coordinates for each source, accounting for proper motion, and we determine the position of the *TESS* observatory with respect to the center of the Earth at the time of each observation using the JPL-Horizons Telnet interface (Giorgini, JD and JPL Solar System Dynamics Group 2023). We confirm that this method reproduces the barycentric corrections listed in the FFI image headers for the sky coordinates corresponding to the listed image positions to within 0.15 s for all observations, with a mean difference between the barycentric corrections that we measure, and those given in the headers, of 0.002 s, and a standard deviation of 0.039 s. Note that if we do not account for the orbit of *TESS* then the barycentric corrections may differ by as much as 1.3 s.

### 3.3. Light Curve Detrending

To facilitate the detection of short time-scale variability it is necessary to apply trend filtering methods to the light curves. The detrending process that we apply differs from what was done by the CDIPS project, which separately applied two different detrending methods: Principle Component Analysis (PCA; e.g., Ivezic et al. 2014), and the Trend Filtering Algorithm (TFA; Kovács et al. 2005). Like CDIPS, we also apply TFA, but we first apply a Spline-based External Parameter Decorrelation (SEPD), which we describe more below, and then we run TFA on the SEPD-filtered light curves. Due to the much larger number of light curves that we are processing here compared to what was handled by CDIPS, we do not apply PCA, which, as an iterative process, is computationally slower than SEPD and TFA. The detrending is carried out using the VARTOOLS program (Hartman & Bakos 2016).

The SEPD method that we apply to the raw light curves involves fitting a linear combination of basis functions to each light curve, and then subtracting the optimal fit. The detrending is performed against four variables: time, the X and Y CCD position of the source, and the temperature of the CCD. Here we use basis splines to remove low frequency variations from the light curves, which for *TESS* tend to be dominated by instrumental systematics, particularly unmodeled scattered light. We use a third order spline with a knot spacing of 1 day, and split the fit into independent bases on any time gaps in the light curve that exceed 0.5 days. This is done to handle significant variations that occur just before and after data downlinks. For the X and Y position and the temperature we use a simple linear relation for the basis functions. In performing the decorrelations we exclude greater than  $3\sigma$  outliers from the fit. This SEPD correction differs from the PCA-based filtering applied by CDIPS in that here the correction includes an explicit decorrelation against time to remove long timescale variations and maximize the ability to detect shorter timescale variations such as eclipses or planetary transits. For longer term variations, filtering methods that are tailored to the specific type of longer variability searched for may be needed, and we therefore choose not to present a generic filtering that is unlikely to be optimal for any particular class of longer period variables.

Note that we did not attempt to quantify the significance of the different detrending factors, nor did we conduct a thorough exploration of other potential factors. Such an exercise may be fruitful, but is beyond the scope of the present paper, which focuses on the delivery of the light curves that have already been produced.

The second detrending that is performed on the SEPD-filtered light curves is an application of the Trend Filtering Algorithm (TFA) of Kovács et al. (2005). Here, for each Sector/Camera/CCD combination a representative list of 200 light curves is randomly selected such that the stars are distributed uniformly across the CCD and uniformly in magnitude. Variable stars are iteratively identified and removed from the list. Each light curve is then fit as a linear combination of the 200 template light curves, and the best-fit model is then subtracted to yield the TFA-corrected light curve. Here we use the same lists of template light curves as used by the CDIPS project for each Sector/Camera/CCD.

We stress again that any variability on timescales longer than 1 day will be filtered from the detrended light curves (columns labelled EPD or TFA in Table 2), and that the pre-detrended light curves should instead be used to study longer period variations (columns labelled IRM in Table 2). For a demonstration of this, see the discussion on Cepheid Variables in Section 4.3.2.

## 4. RESULTS

### 4.1. Summary of Available Data

A total of 83,717,159 light curves from *TESS* Cycle 1 (Sectors 1 through 13) for 56,401,549 stars are being made available through the NASA Mikulski Archive for Space Telescopes (MAST) as a High Level Science Product via <http://doi.org/10.17909/8nxx-tw70><sup>1</sup>. Stars closer to the Southern ecliptic pole have observations from multiple sectors, and will have more than one *TESS* Cycle 1 light curve produced by our project. The light curves are provided in binary FITS table format, with the light curves organized by Sector, Camera, and CCD. The Gaia DR2 identifier is included in the name of each light curve. The data columns included in each light curve file are described in Table 2.

Note that the  $S$ ,  $D$  and  $K$  parameters included in the light curve come from fitting an elliptical Gaussian to the stellar profile. The elliptical Gaussian,  $F$ , has the form:

$$F = A \exp\left(-\frac{1}{2}B\right) \quad (2)$$

$$B = S((\Delta x)^2 + (\Delta y)^2) + D((\Delta x)^2 - (\Delta y)^2) + 2K\Delta x\Delta y \quad (3)$$

where  $A$  is the amplitude of the profile, and  $\Delta x$  and  $\Delta y$  are the  $x$  and  $y$  distances, in pixels, from the center of the profile.

<sup>1</sup> <https://archive.stsci.edu/hlsp/t16/>

**Table 2.** Data columns included in light curve files produced by the T16 project

| Column Name | FITS Data Type | Column Description   |
|-------------|----------------|--|
| RSTFC       | 17A            | TESS image identifier  |
| TMID.UTC    | D              | UTC-based Julian Date mid exposure time minus 2457000                        |
| TMID.BJD    | D              | TDB-based Barycentric Julian Date mid exposure time minus 2457000            |
| BGV         | D              | Background value at the location of the source                               |
| BGE         | D              | Background measurement error   |
| FSV         | D              | Measured value of S parameter characterizing the PSF (Eq. 2)                 |
| FDV         | D              | Measured value of D parameter characterizing the PSF (Eq. 2)                 |
| FKV         | D              | Measured value of K parameter characterizing the PSF (Eq. 2)                 |
| IFL1        | D              | Flux in 1.0 pixel aperture in Analog-to-Digital Units (ADU)                  |
| IFL2        | D              | Flux in 1.5 pixel aperture in ADU  |
| IFL3        | D              | Flux in 2.25 pixel aperture in ADU   |
| IFE1        | D              | Flux uncertainty in 1.0 pixel aperture in ADU                                |
| IFE2        | D              | Flux uncertainty in 1.5 pixel aperture in ADU                                |
| IFE3        | D              | Flux uncertainty in 2.25 pixel aperture in ADU                               |
| IRM1        | D              | Instrumental magnitude in 1.0 pixel aperture in magnitude units              |
| IRM2        | D              | Instrumental magnitude in 1.5 pixel aperture in magnitude units              |
| IRM3        | D              | Instrumental magnitude in 2.25 pixel aperture in magnitude units             |
| IRE1        | D              | Instrumental magnitude uncertainty in 1.0 pixel aperture in magnitude units  |
| IRE2        | D              | Instrumental magnitude uncertainty in 1.5 pixel aperture in magnitude units  |
| IRE3        | D              | Instrumental magnitude uncertainty in 2.25 pixel aperture in magnitude units |
| EPD1        | D              | Spline-EPD detrended magnitude in 1.0 pixel aperture                         |
| EPD2        | D              | Spline-EPD detrended magnitude in 1.5 pixel aperture                         |
| EPD3        | D              | Spline-EPD detrended magnitude in 2.25 pixel aperture                        |
| TFA1        | D              | TFA-detrended magnitude in 1.0 pixel aperture                                |
| TFA2        | D              | TFA-detrended magnitude in 1.5 pixel aperture                                |
| TFA3        | D              | TFA-detrended magnitude in 2.25 pixel aperture                               |
| XPOS        | D              | X image position of source on subtracted frame                               |
| YPOS        | D              | Y image position of source on subtracted frame                               |
| TEMP        | D              | mean CCD temperature in K  |
| NTEMPS      | D              | The number of temperatures averaged to compute TEMP                          |

#### 4.2. Photometric Precision

To characterize the photometric precision attained through this work, we calculate the median absolute deviation (MAD) of each magnitude time-series for each source, where we take

$$\text{MAD} = \text{med}_i(|\text{mag}_i - \text{med}_j(\text{mag}_j)|) \quad (4)$$

to be the median of the absolute differences from the median. Figures 1 and 2 show the  $1.483 \times \text{MAD}$  vs. T-band magnitude for light curves from a selected sample of sector/camera/ccd combinations. Here the scaling factor of 1.483 is chosen as the expected value  $1.483 \times \text{MAD}$  is equal to the standard deviation for a Gaussian distribution, in the large sample limit. A full set of figures showing these relations for all sector/camera/ccd combinations is available at <https://doi.org/10.5281/zenodo.14278698>. Shown in these figures are estimates for the theoretically expected photometric noise floor, as calculated in Bouma et al. (2019). Individual contributions from the source shot noise, from the sky background due to unresolved stars, from read-noise, and a systematic noise floor, are shown as the various dashed lines in the figure.

In general, without detrending, the scatter in the light curves, as measured by MAD, is significantly above the theoretical noise floor. This is due to the large systematic variations present in the light curves, especially near times in the orbit with high and complex background scattering. Figure 3 demonstrates this for the undetrended light curves from the two sectors shown in Fig 1. Here we calculate the median MAD of the aperture 3 light curves for stars within the magnitude range  $9 < T < 10$  in 0.5 d time bins, and show the result as a function of time from the first observation in the sector. For both sector/camera/ccd combinations shown the MAD shows pronounced increases at specific times in the light curves, but the outliers are particularly noticeable for the Sector 8, Camera 4, CCD 3. After applying the SEPD and TFA detrending techniques the noise for most stars in most sector/camera/ccd combinations approaches the theoretical noise floor.

There are several notable exceptions, such as Sector 8, Camera 4, CCD 3 which is shown in Figure 1. The T16 light curves derived for this sector/camera/ccd exhibit systematic and sudden jumps to lower brightness that can last for up to 3 days. This may be related to the presence of a bad column on the CCD and the bright

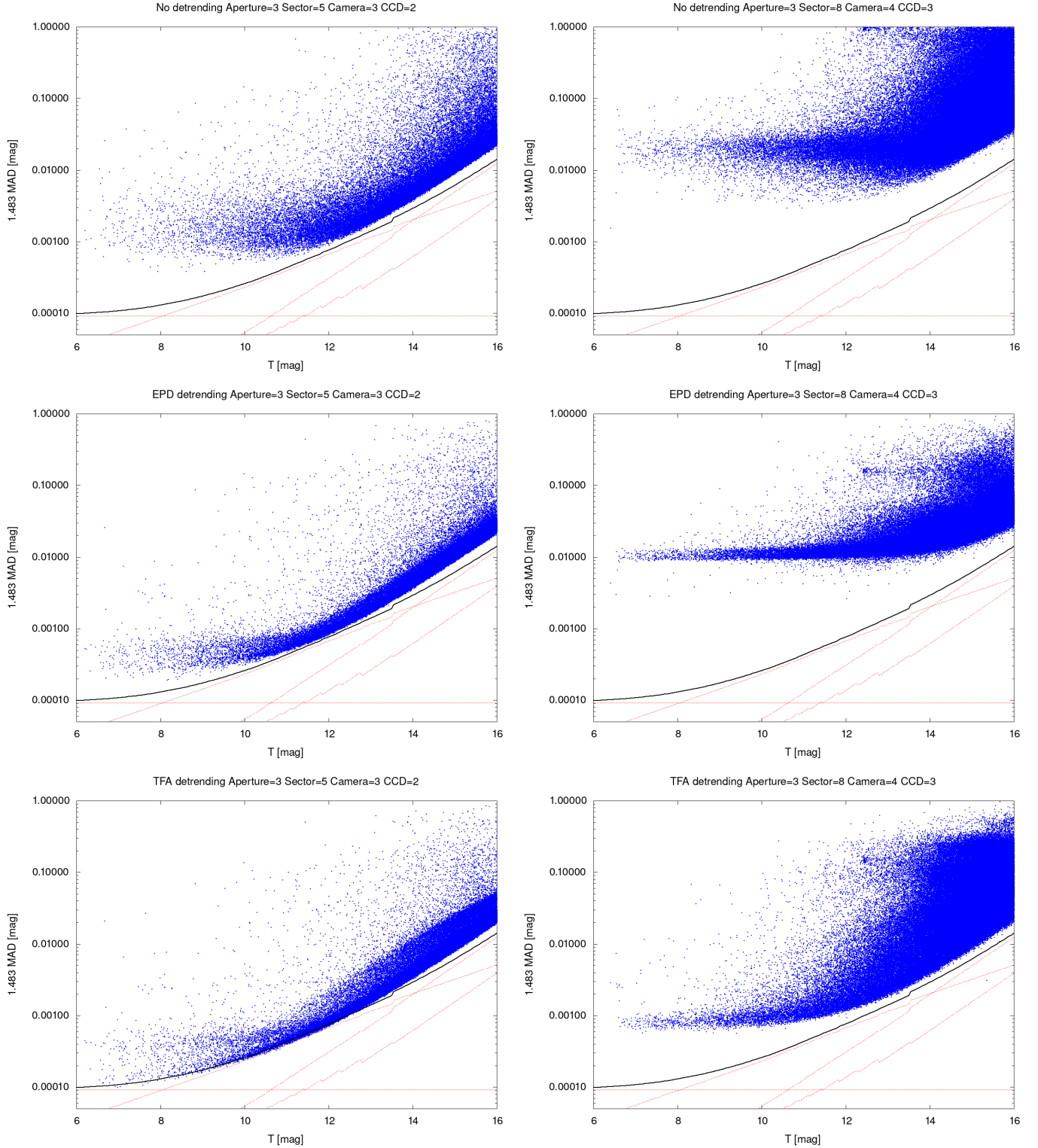


**Figure 1.** The T16 aperture 3 light curve MAD plotted vs the source  $T$ -band magnitude for a Sector/Camera/CCD where the precision approaches the theoretical noise floor after detrending (*left*), and for the Sector/Camera/CCD with the poorest realized precision (*right*). See Section 4.2 for a discussion of why the systematic noise floor is so high for this particular dataset. The solid line shows the theoretical noise floor from Bouma et al. (2019), while the dashed lines show contributions from the source shot noise, background shot noise, and detector read noise. The top row shows the statistics for the un-detrended light curves, the middle row for the SEPD-detrended light curves, and the bottom row for the SEPD+TFA-detrended light curves. Even for Sector/Camera/CCD combinations where the theoretical noise floor is achieved, as shown at left, there are often some light curves in the data with higher levels of systematic errors.

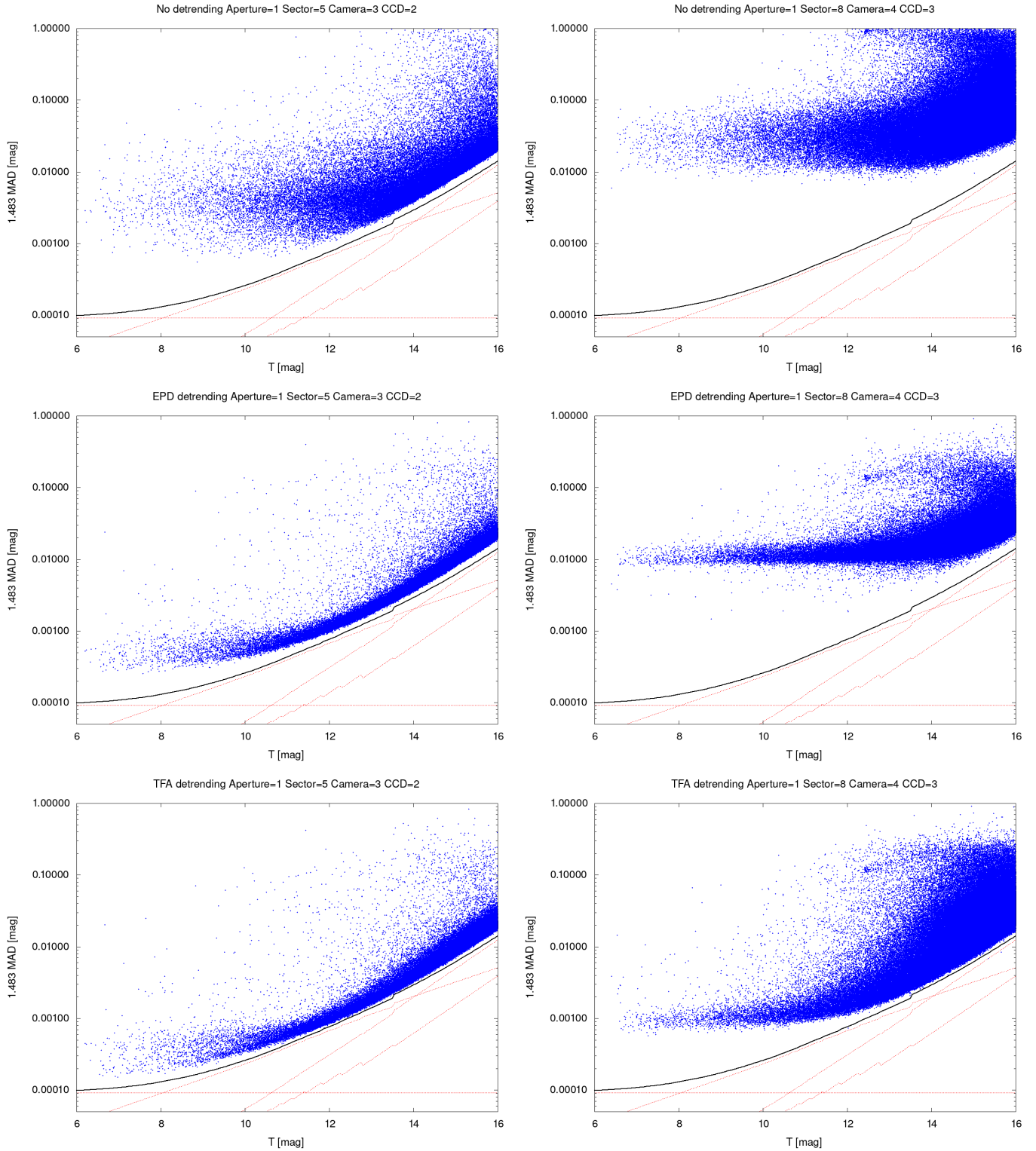


**Figure 2.** Similar to Fig. 1, here we show the results for aperture 1. As expected, the precision for fainter stars improves using the smaller aperture, while for brighter stars the larger aperture yields improved precision.

star  $\beta$  Dor which bled into the upper buffer rows of the CCD according to the *TESS* data release notes for Sec-

tor 8. One or both of these features may have impacted the image subtraction process fit for the change in flux



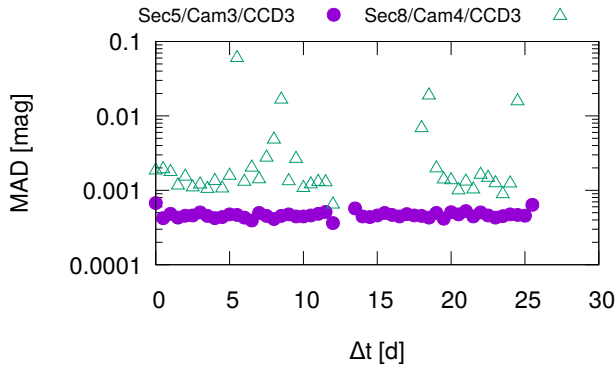


**Figure 3.** The median MAD vs. time from the first observation in a sector for stars with  $9 < T < 10$  in the two indicated sector/camera/ccd combinations (the same as those shown in Fig. 1). The MAD is calculated in 0.5 day bins for each light curve using the undetrended aperture 3 magnitudes. The MAD is systematically higher at specific times, especially at points in the spacecraft orbit with high and complex background scattering.

scale between the reference and science images. An inspection of the subtracted frames shows sudden jumps in the flux residuals across the entire CCD that suggests a bad fit to the dataset at these times. We present this here to caution the user that data anomalies are present in these data, leading in some cases to large systematic artifacts that are especially pronounced for particular sector/camera/ccd combinations. In addition to sector 8, camera 4, ccd 3, two other datasets exhibit a systematic noise floor above 0.5 mmag. These are sector 1, camera 2, ccds 2 and 4. The user is encouraged to inspect the magnitude-MAD diagrams for any particular sector/camera/ccd that they wish to use to aid in evaluating the significance of systematic photometric errors for those data.

Figure 4 shows the 10th percentile, median, and 90th percental MAD for the pre-detrending raw photometry light curves at different  $G$ -band magnitudes as a function of position on the sky. For bright stars (e.g., the  $8.0 < T < 8.5$  range shown in the Figure, corresponding to stars close to saturation) we find that undetrended light curves are dominated by systematic errors, the level of which varies significantly among the different Sector/Camera/CCD combinations. For some combinations of Sector/Camera/CCD the median MAD is as high as  $\sim 0.1$  mag for these bright stars, while for others the median MAD is less than 0.001 mag. This gives rise to the regions of high MAD that are localized on the sky, and uncorrelated with Galactic latitude. For fainter stars (e.g.,  $15 < T < 15.5$ ) noise from the sky

background dominates, and the median MAD is highest near the Galactic plane.

Figures 5 and 6 show similar plots for the SEPD, and TFA-detrended light curves, respectively. SEPD and TFA progressively reduce the MAD for the bright stars, with most Sector/Camera/CCD combinations showing median MAD values below 0.001 mag after SEPD, and all but one combination (Sector 1, Camera 2, CCD 4) having a median MAD below this level after TFA. For the fainter stars the difference between the undetrended, SEPD and TFA precision is less pronounced, as expected for white-noise dominated light curves.

Figures 7, 8, and 9 similarly show the ratio of the MAD to the expected MAD on the sky at the 10th, median and 90th percentile levels for the raw, SEPD, and TFA-detrended light curves, respectively. For the faintest stars away from the Galactic plane, the measured MAD is close to the expected MAD before detrending, while for bright stars the pre-detrending MAD is much higher than ( $\gtrsim 100$  times) the expected MAD, but approaches the expected MAD after TFA-detrending.

#### 4.3. Comparison to Other Reductions

We compare our light curves to the available FFI light curves produced by four of the other projects listed in Table 1. Here we restrict the comparison to projects that aim for a broad selection of stars, and do not compare to the PATHOS or DIAMANTE projects that have released light curves only for star cluster members and transiting planet hosts. We also do not compare to the CDIPS project, since we are making direct use of the CDIPS reduction pipeline. Here we do a thorough comparison for all sectors, cameras, and CCDs to the SPOC-TESS and QLP projects. For the TGLC and GSFC-ELEANOR-LITE projects, which have very large data volumes, we selected 1% of the light curves for comparison. To ensure a uniform sampling in magnitude and position on the sky, we made use of the batch light curve download scripts for these projects provided by MAST, downloading every hundredth file listed in the scripts.

##### 4.3.1. Precision Comparison

To perform the comparison we obtained the light curves from each of these projects from MAST. We then compute the MAD for each light curve in all available methods and states of trend-filtering. For the QLP light curves we compute this for both the simple aperture photometry (SAP column in the available FITS files) and Kepler-Spline simple aperture photometry (KSP-SAP column) time series, while for SPOC-TESS we compute this for both the SAP and pre-search data conditioning simple aperture photometry (PDCSAP column)

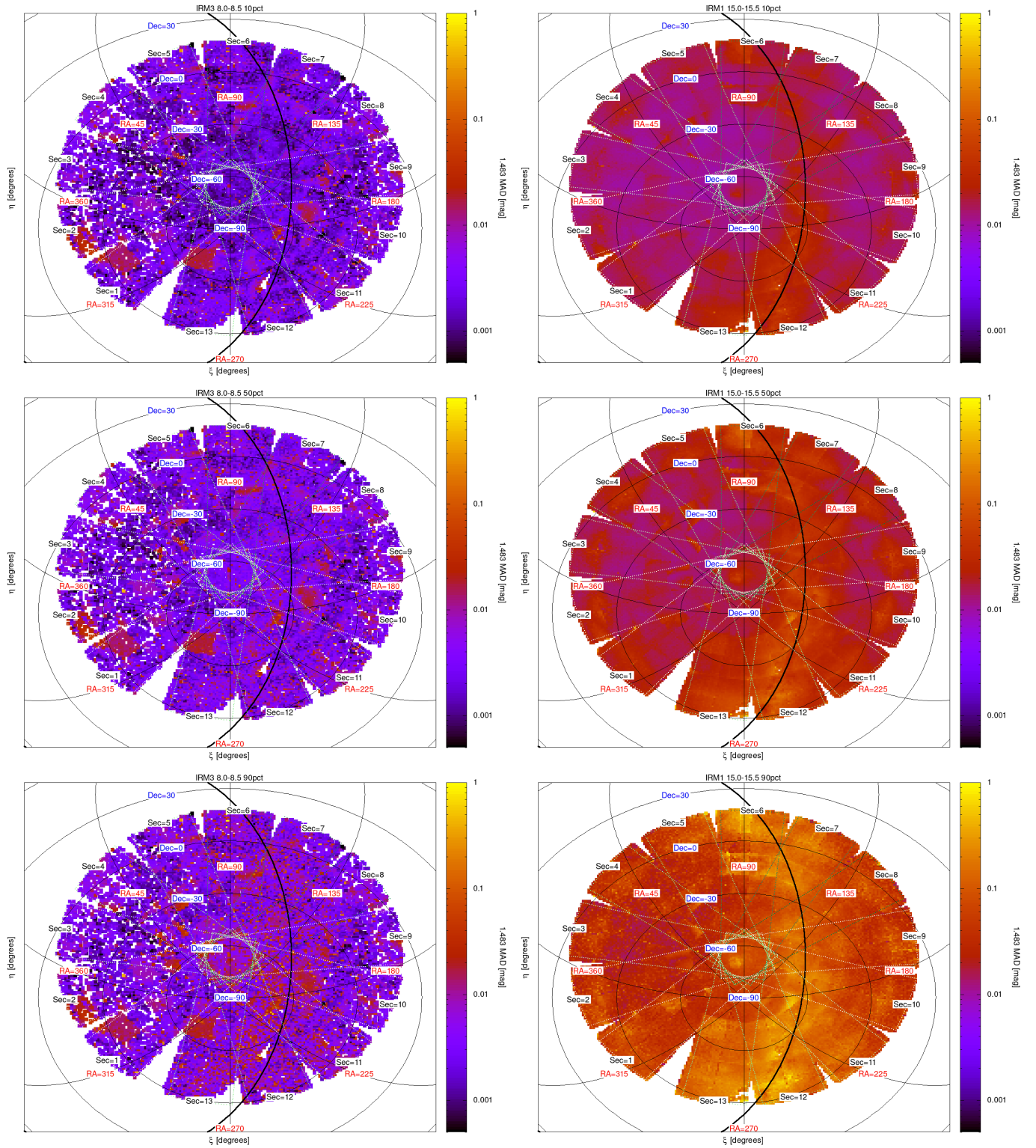


**Figure 4.** The 10th percentile (top), median (middle) and 90th percentile (bottom) MAD for pre-detrended light curves calculated for bins in sky position and magnitude. The results are displayed using an arc-projection about the south ecliptic pole. We scale the MAD by a factor of 1.483 so that the expected value is equal to the standard deviation for a Gaussian distribution. Here we show the results for stars with  $8 < T < 8.5$  (left) and  $15 < T < 15.5$  (right). The sector boundaries are shown and labelled, as are lines of constant right ascension and declination. The dark black line in each panel shows the Galactic plane. For faint stars the MAD is dominated by the background shot noise which is higher along the plane, while for brighter stars the scatter is dominated by instrumental systematics which depend strongly on the Sector/Camera/CCD.

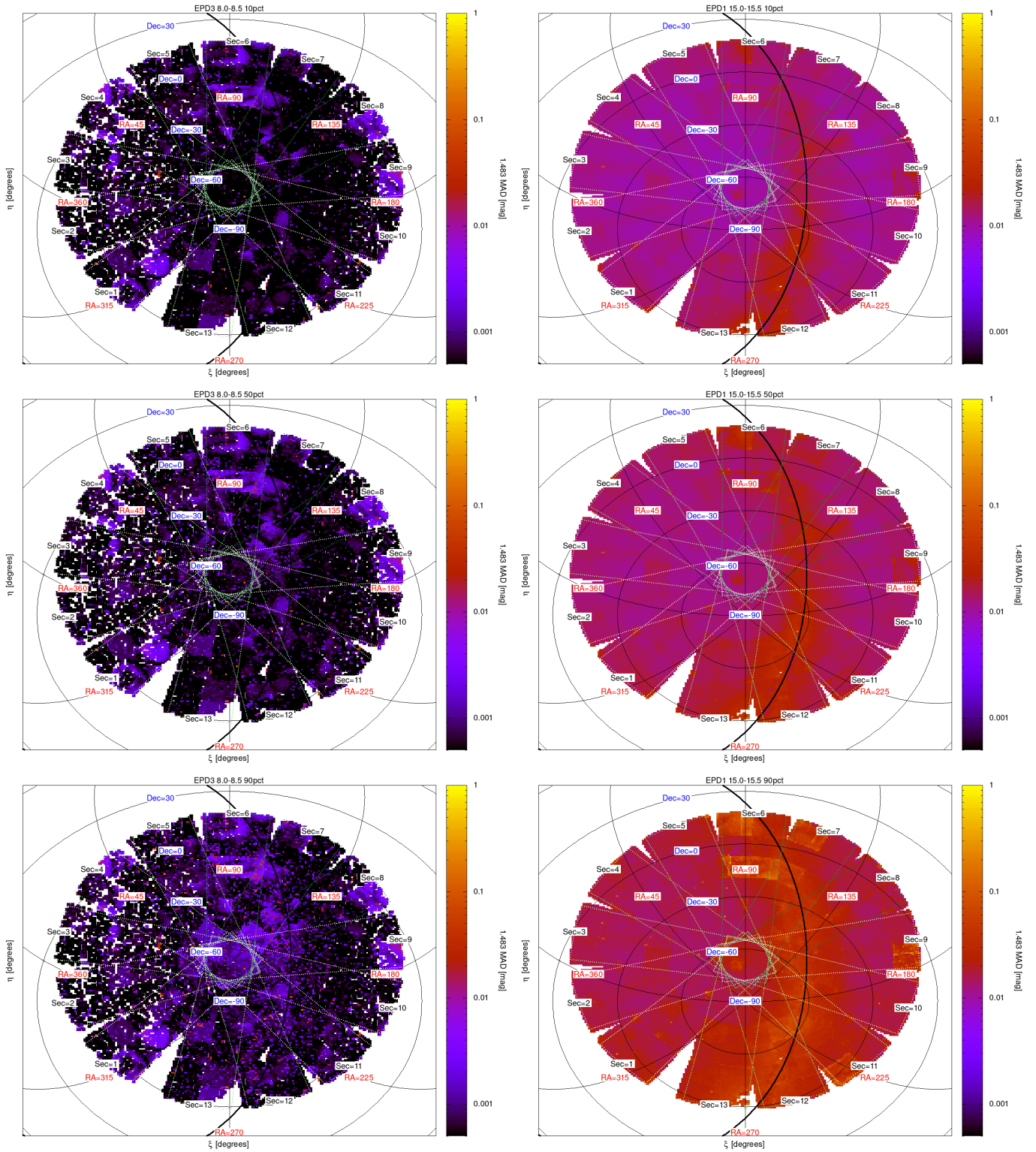


**Figure 5.** Same as Figure 4, here we show the statistics for SEPD light curves.

time series data. For TGLC we compute the MAD for the PSF-fitting photometry (psf\_flux column), aperture photometry (aperture\_flux), calibrated PSF-fitting pho-

tometry (cal\_psf\_flux), and calibrated aperture photometry (cal\_aper\_flux) time series. For GSFC-ELEANOR-LITE we use the raw flux (RAW\_FLUX) and corrected

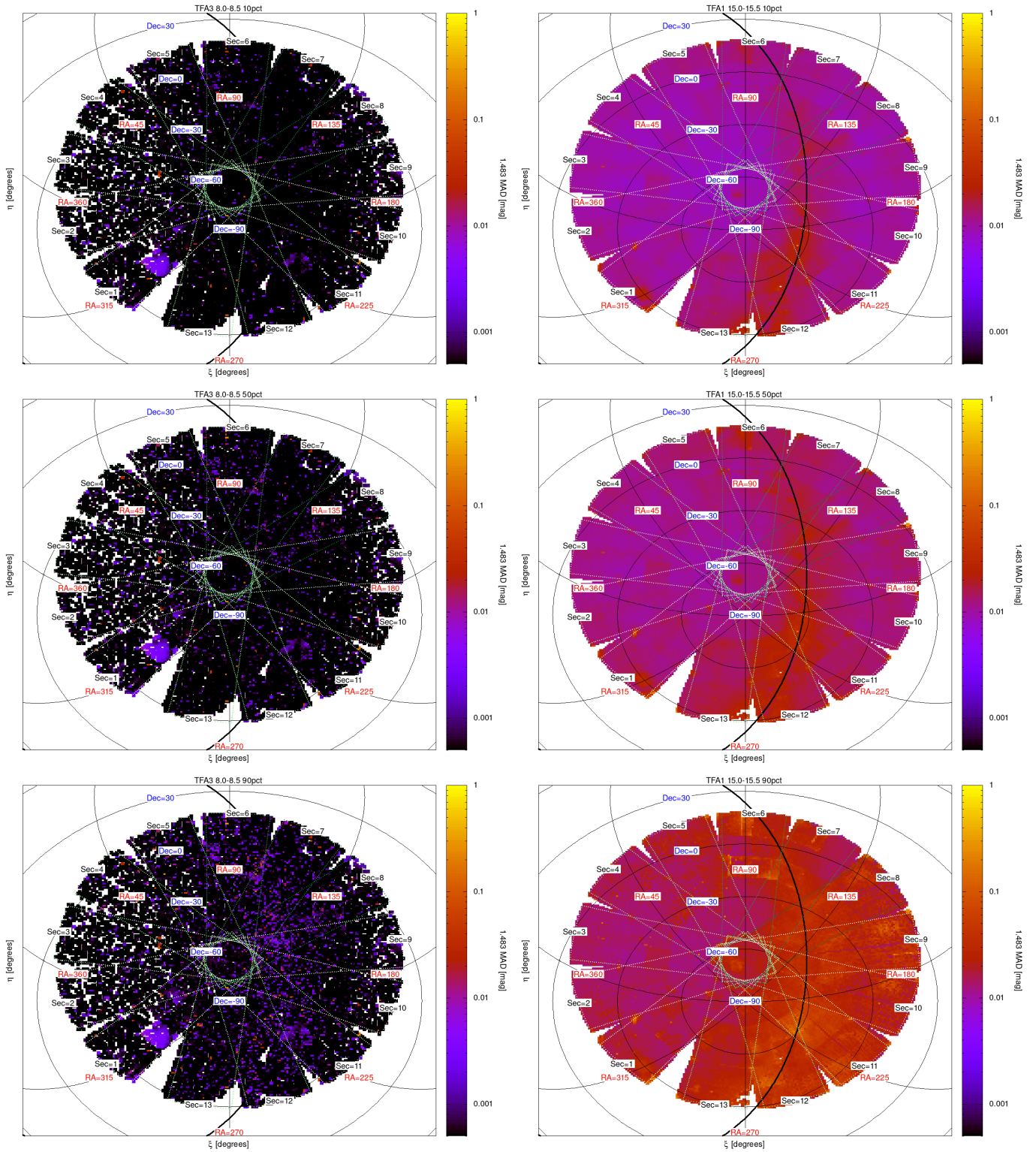


**Figure 6.** Same as Figure 4, here we show the statistics for TFA light curves.

flux (CORRECTED\_FLUX) time series. In all cases we exclude any data point that is flagged as being potentially affected by some instrumental artifact.

Note that because each project applied a different detrending method, the precision comparison that we are performing here should not be interpreted as a pure com-

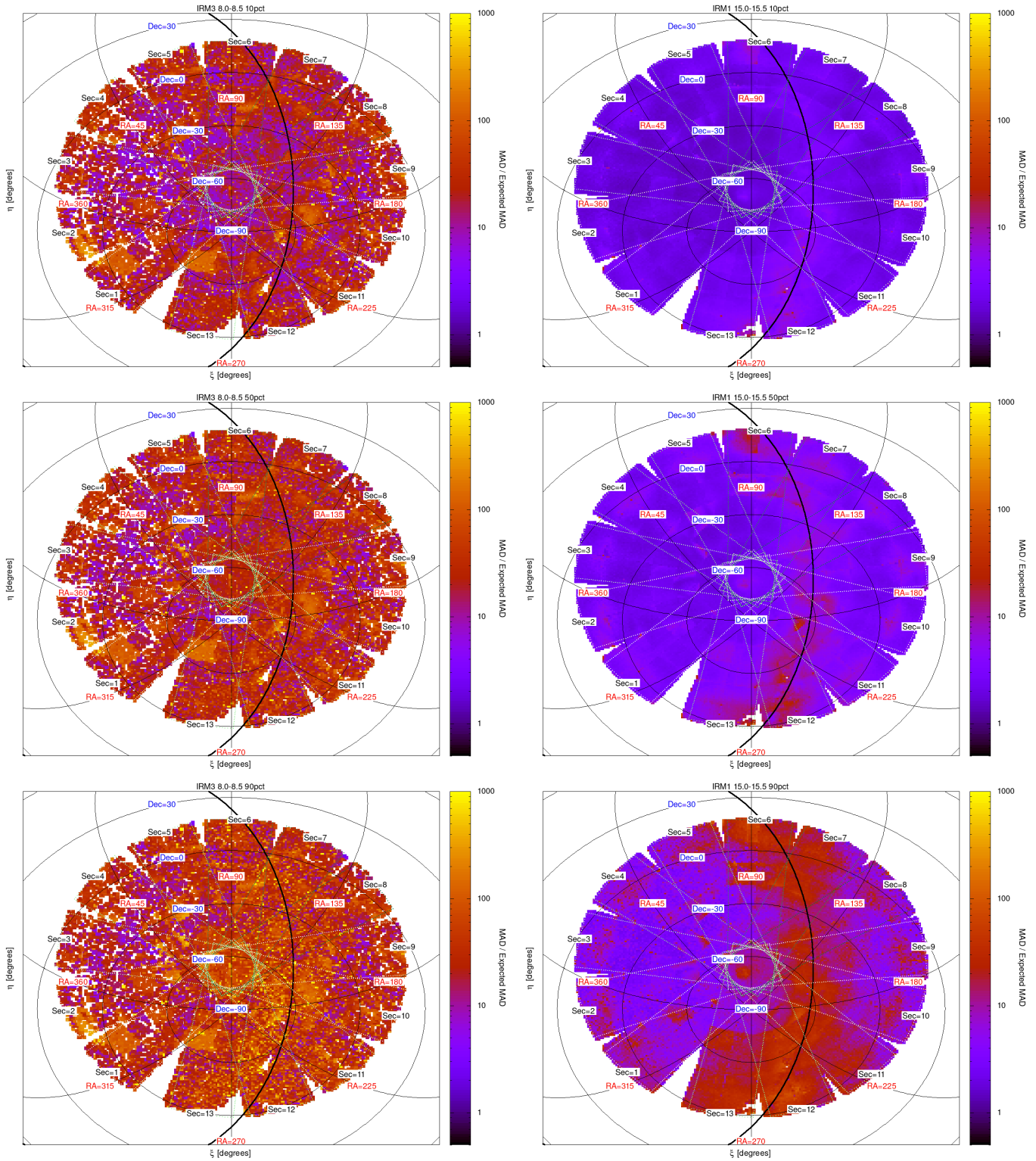


**Figure 7.** Same as Figure 4, here we show the ratio of the MAD to the expected MAD.

parison of the different photometry methods or of the different detrending methods, but is rather a comparison of the different combined photometry+detrending

methods. The goal here is to compare the precision of the different light curves that are readily available to the

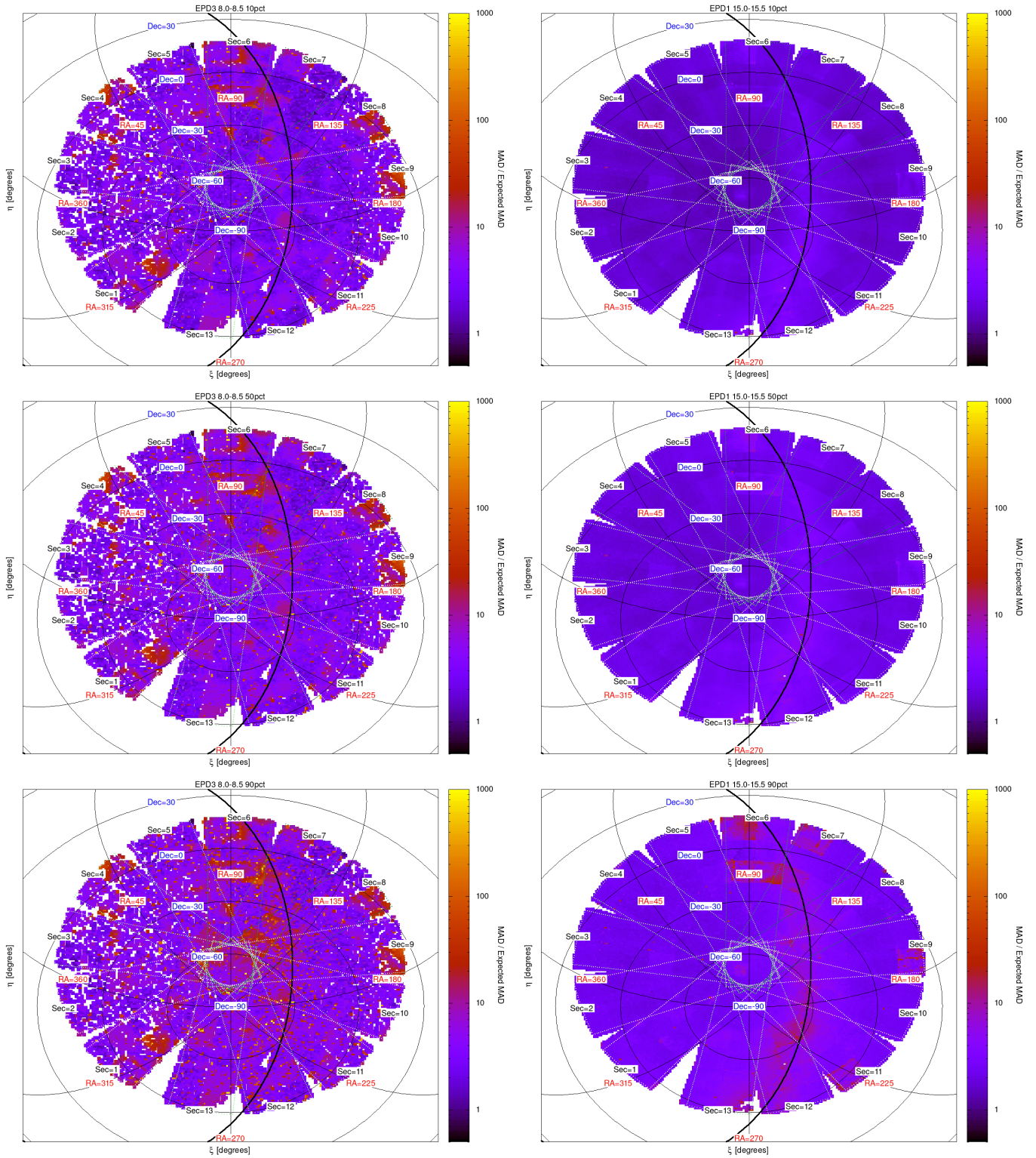


**Figure 8.** Same as Figure 5, here we show the ratio of the MAD to the expected MAD.

public, and not to compare the individual stages of the reduction methods.

Figure 10 compares the T16 light curve precision to the QLP precision, Figure 11 shows this comparison for the SPOC-FFI light curves, Figure 12 shows the com-

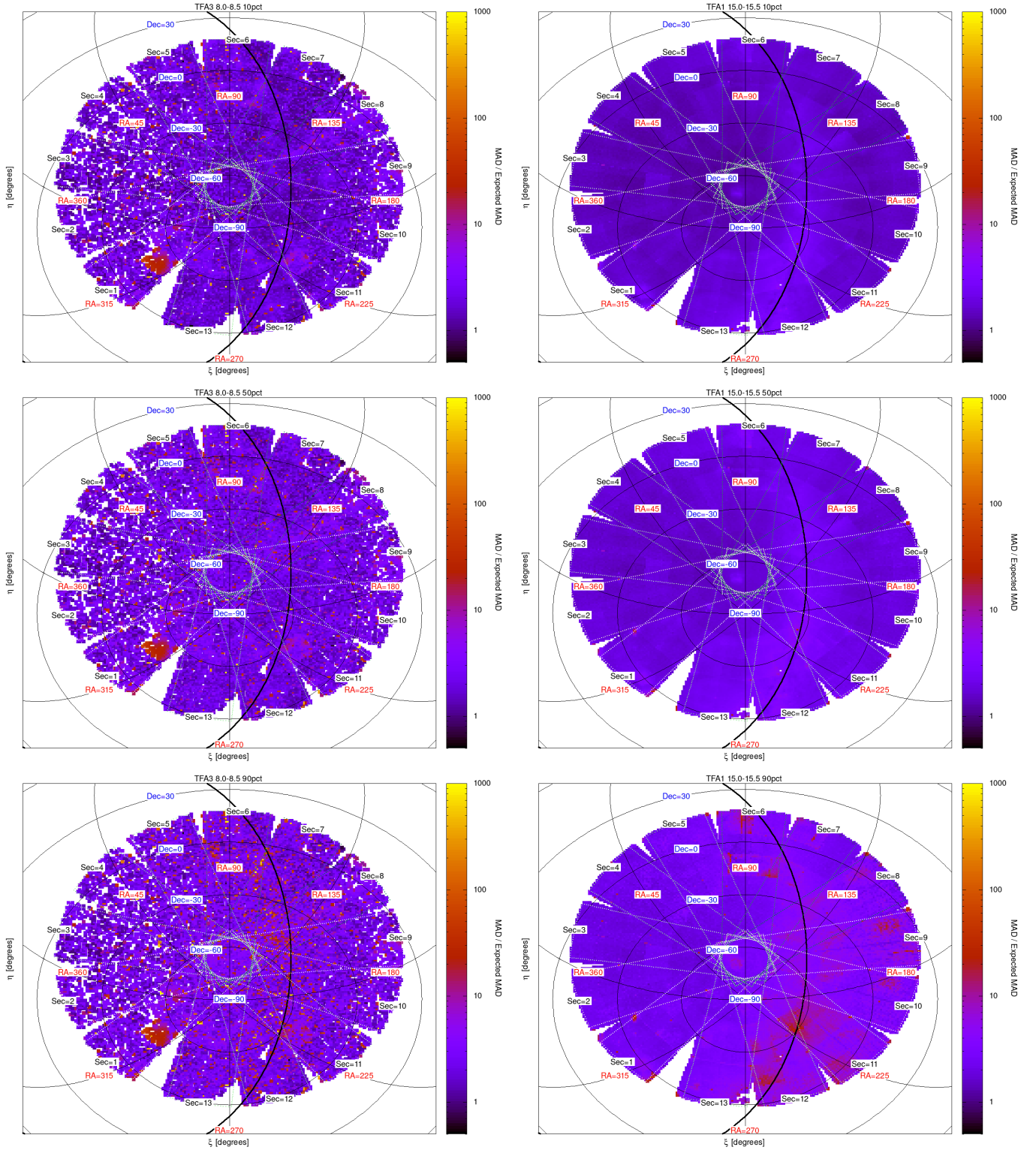


**Figure 9.** Same as Figure 6, here we show the ratio of the MAD to the expected MAD.

parison for the GSFC-ELEANOR-LITE light curves, and Figure 13 shows the comparison for the TGLC light curves. A figure set that shows these compar-

isons for every *TESS* sector, camera, and CCD combination, for each of the three photometric apertures that we employ, for the IRM, EPD and TFA light

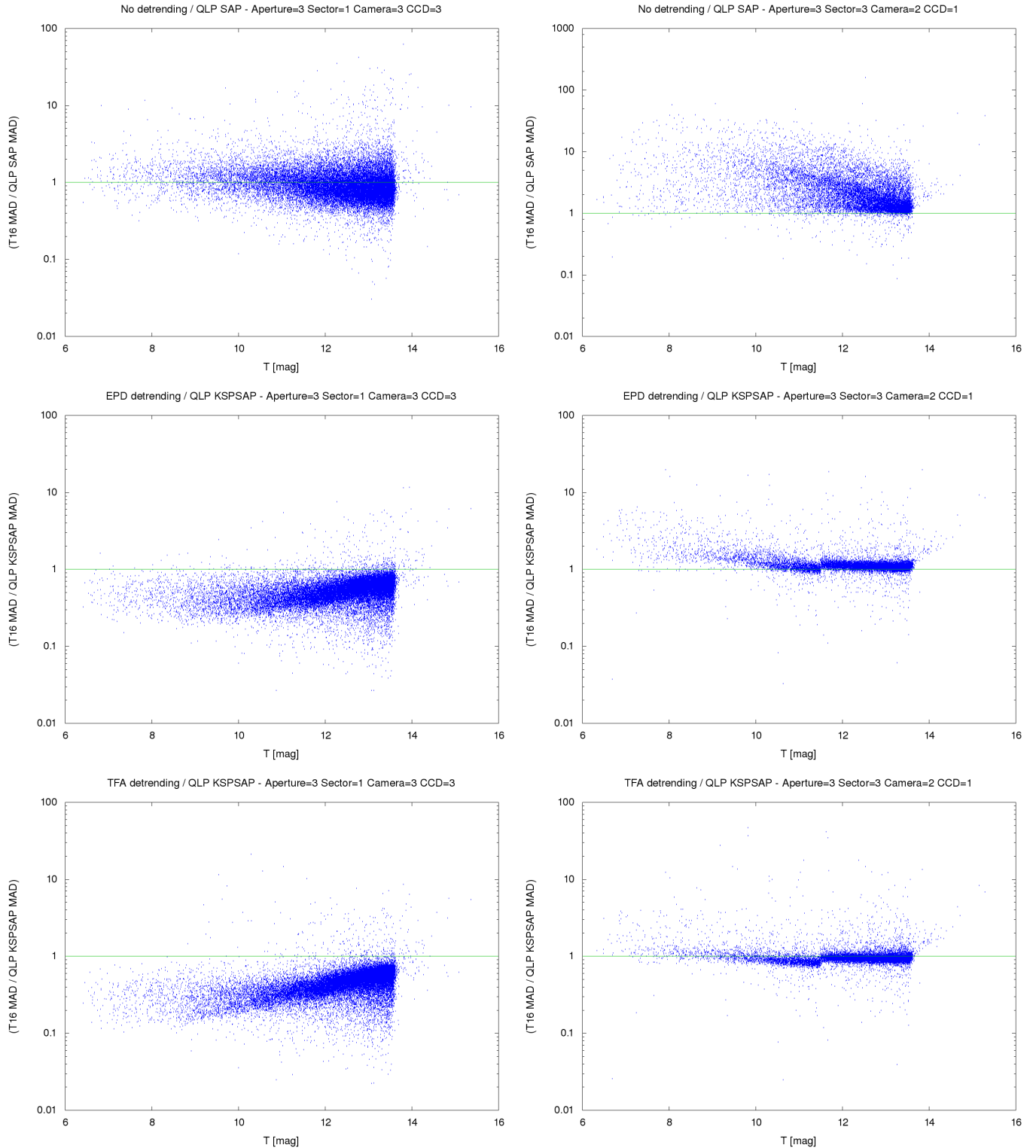


**Figure 10.** The ratio of the T16 light curve MAD to the QLP light curve MAD, for a Sector/Camera/CCD where the T16 light curves have systematically lower MAD than QLP (*Left*), and for a Sector/Camera/CCD where the un-detrended QLP light curves have systematically lower MAD than the un-detrended T16 light curves (*right*). We show the comparison only for aperture 3 of the T16 light curves. For smaller apertures the precision of the T16 light curves tends to get worse for brighter stars and better for fainter stars, so the ratio shown here is lower at the bright end than it is for apertures 1 or 2, but higher at the faint end than it is for the other apertures. In the *top* row we compare the un-detrended T16 light curve precision to the un-detrended QLP light curve precision. In the *middle* row we compare the SEP-detrended T16 light curve precision to the KSPSAP detrended QLP light curve precision. In the *bottom* row we compare the TFA-detrended T16 light curve precision to the KSPSAP detrended QLP light curve precision.



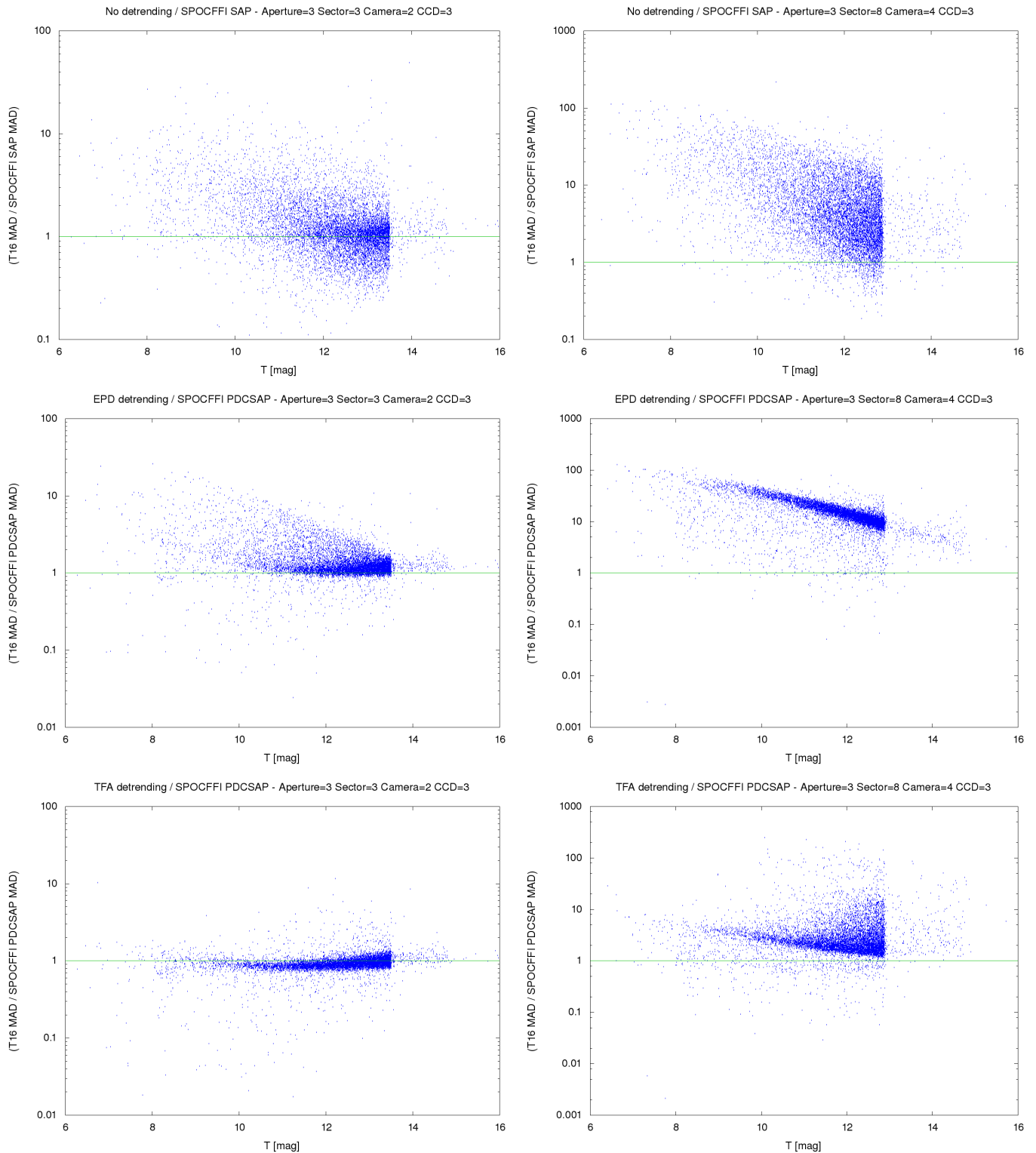


**Figure 11.** Similar to Fig. 10, here we compare the T16 light curve MAD to the SPOC-FFI light curve MAD. The Sector/Camera/CCD combinations shown here differ from those shown in Fig. 10.

curves from T16, and for all of the different photometric time series provided on MAST is available at

<https://doi.org/10.5281/zenodo.14278698>. In this

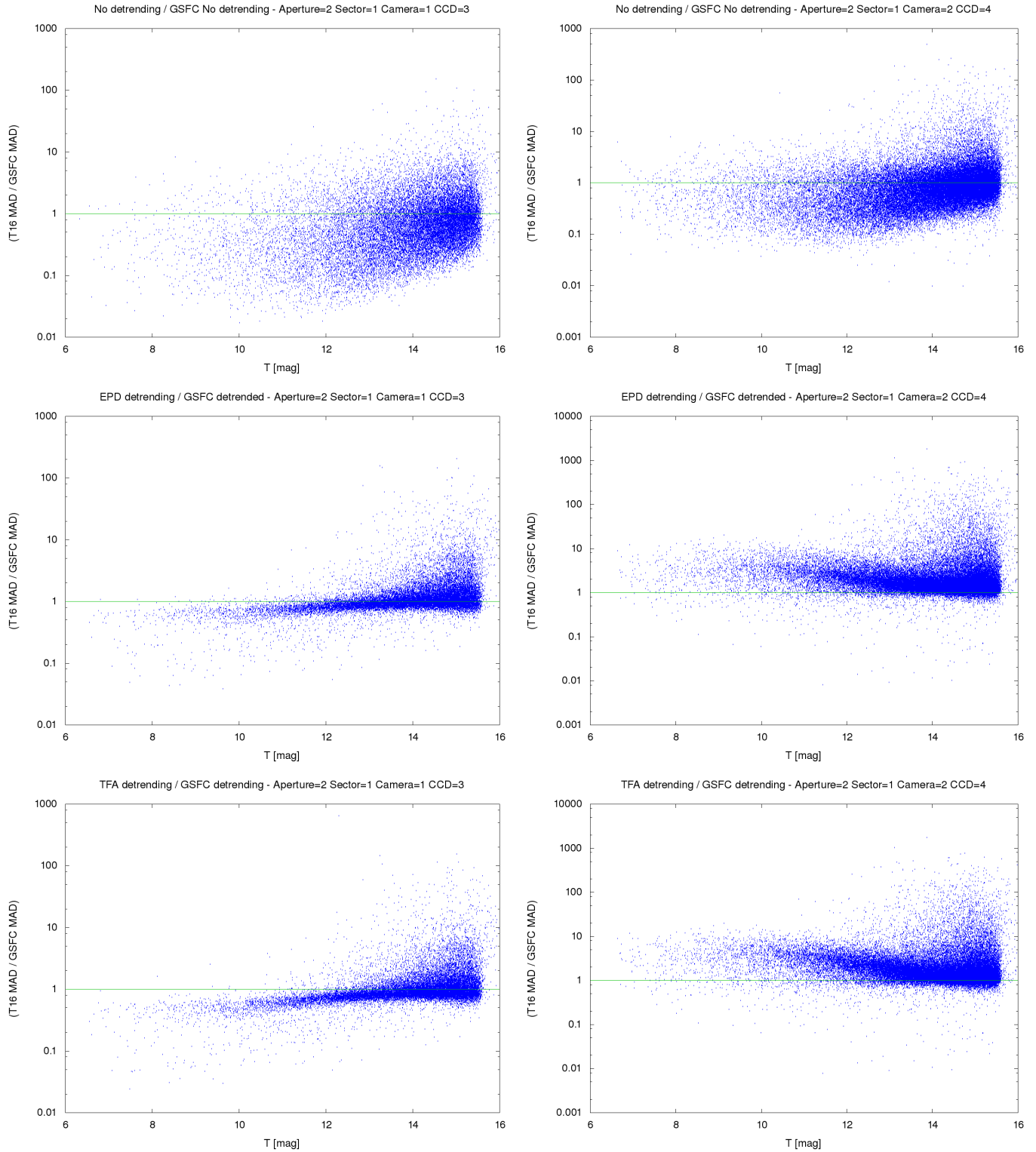


**Figure 12.** Similar to Fig. 10, here we compare the T16 light curve MAD to the GSFC-ELEANOR-LITE light curve MAD. The Sector/Camera/CCD combinations shown here differ from those shown in Fig. 10. We also use aperture 2 for T16 rather than aperture 3.

article we show a small subset of these different comparison plots.

Table 3 compares the precision of the T16 light curves to that of the QLP, SPOC-TESS, GSFC and TGLC light

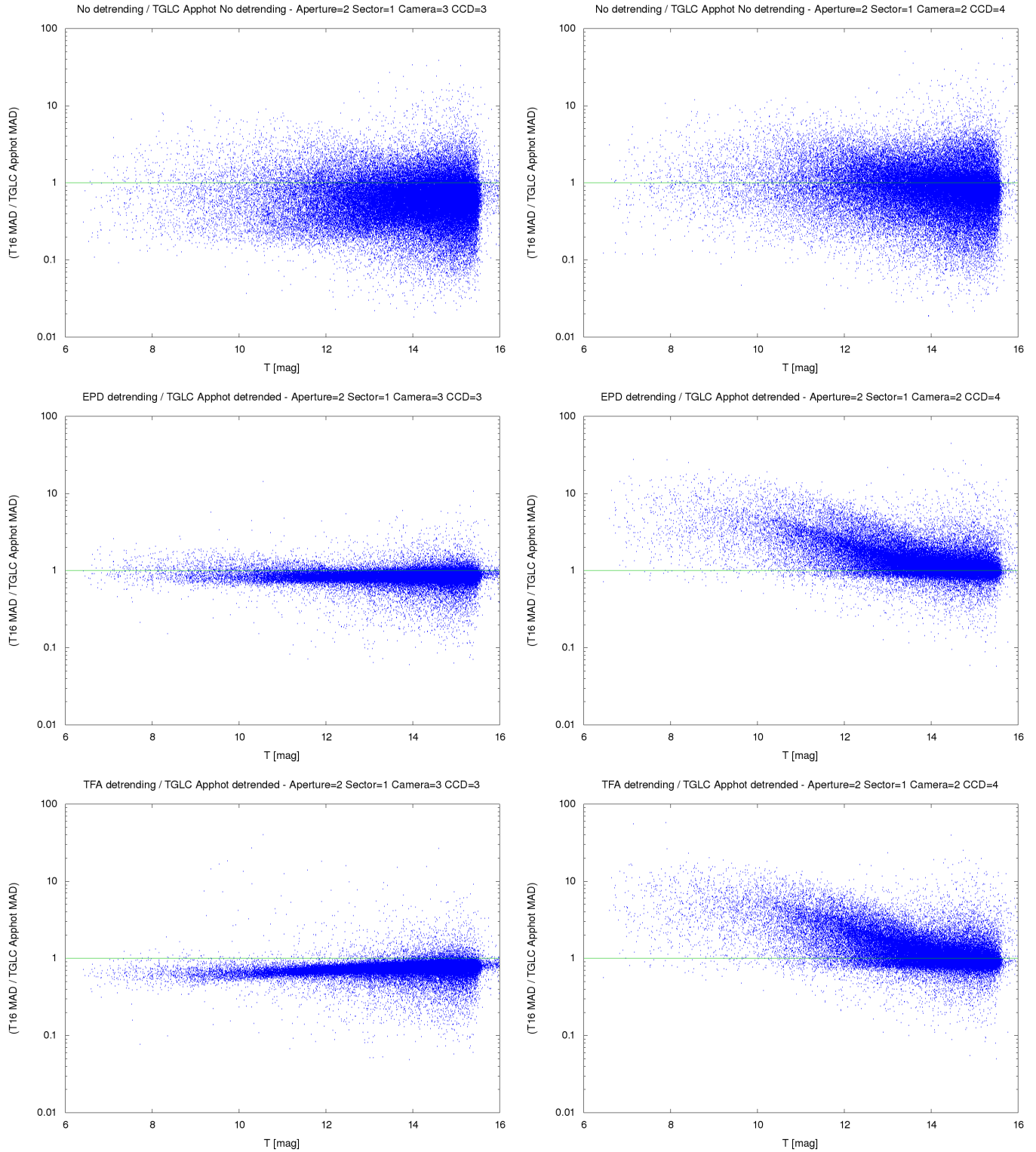


**Figure 13.** Similar to Fig. 10, here we compare the T16 light curve MAD to the TGLC aperture photometry light curve MAD. Note that the TGLC aperture photometry has systematically better precision than the PSF photometry for sector 1, so we restrict the comparison shown here to the aperture photometry. The Sector/Camera/CCD combinations shown here differ from those show in Fig. 10. We also use aperture 2 for T16 rather than aperture 3.

curves by listing the fraction of light curves by Sector for which the T16 light curves has a lower MAD than

**Table 3.** Fraction of light curves with T16 MAD lower than MAD from other projects by sector

| Sector       | QLP <sup>a</sup> | QLP <sup>b</sup> | SPOC-FFI <sup>a</sup> | SPOC-FFI <sup>b</sup> | GSFC <sup>a,c</sup> | GSFC <sup>b,c</sup> | TGLC <sup>a,c</sup> | TGLC <sup>a,c</sup> | TGLC <sup>b,c</sup> | TGLC <sup>b,c</sup> |
|--------------|------------------|------------------|-----------------------|-----------------------|---------------------|---------------------|---------------------|---------------------|---------------------|---------------------|
|              | SAP              | KSPSAP           | SAP                   | PDCSAP                | Raw                 | Corrected           | Aperture            | PSF                 | Cal. Aperture       | Cal. PSF            |
| 1            | 60.6%            | 95.5%            | 38.5%                 | 62.9%                 | 66.8%               | 47.1%               | 82.1%               | 75.4%               | 88.8%               | 80.3%               |
| 2            | 11.7%            | 82.7%            | 32.8%                 | 75.0%                 | 58.1%               | 45.7%               | 56.1%               | 67.0%               | 84.1%               | 77.9%               |
| 3            | 17.3%            | 87.1%            | 39.2%                 | 84.1%                 | 83.0%               | 79.2%               | 79.2%               | 83.5%               | 95.3%               | 89.8%               |
| 4            | 8.6%             | 75.3%            | 54.0%                 | 76.7%                 | 71.0%               | 55.3%               | 76.9%               | 81.2%               | 84.7%               | 80.8%               |
| 5            | 20.7%            | 76.0%            | 40.5%                 | 70.6%                 | 67.2%               | 36.2%               | 67.6%               | 76.8%               | 78.0%               | 72.4%               |
| 6            | 25.1%            | 78.1%            | 41.4%                 | 78.4%                 | 51.4%               | 23.3%               | 65.4%               | 69.0%               | 81.3%               | 74.8%               |
| 7            | 30.1%            | 86.4%            | 42.8%                 | 82.8%                 | 55.4%               | 20.2%               | 72.6%               | 71.1%               | 84.9%               | 76.4%               |
| 8            | 14.6%            | 54.8%            | 43.2%                 | 56.8%                 | 58.7%               | 38.1%               | 70.4%               | 70.0%               | 53.2%               | 52.3%               |
| 9            | 28.0%            | 73.1%            | 46.6%                 | 63.9%                 | 55.5%               | 34.5%               | 62.9%               | 62.6%               | 68.1%               | 61.9%               |
| 10           | 29.6%            | 85.1%            | 44.6%                 | 78.8%                 | 57.4%               | 46.8%               | 59.7%               | 57.4%               | 81.0%               | 74.0%               |
| 11           | 23.7%            | 65.9%            | 31.4%                 | 51.1%                 | 51.4%               | 41.6%               | 57.5%               | 51.4%               | 50.7%               | 48.2%               |
| 12           | 42.7%            | 83.6%            | 36.0%                 | 59.0%                 | 57.4%               | 42.0%               | 85.5%               | 75.6%               | 75.7%               | 64.0%               |
| 13           | 33.1%            | 86.3%            | 28.4%                 | 71.7%                 | 67.7%               | 51.2%               | 85.6%               | 73.6%               | 89.9%               | 75.4%               |
| <b>Total</b> | <b>28.8%</b>     | <b>78.0%</b>     | <b>40.0%</b>          | <b>69.8%</b>          | <b>62.3%</b>        | <b>43.1%</b>        | <b>79.5%</b>        | <b>73.7%</b>        | <b>85.6%</b>        | <b>77.3%</b>        |

<sup>a</sup> Comparing to the Undetrended T16 Photometry<sup>b</sup> Comparing to the TFA-detrended T16 Photometry<sup>c</sup> For GSFC and TGLC the comparison is done on a randomly selected subset of the light curves.

the comparison light curves. For SPOC-TESS and QLP we perform this comparison for all available light curves, while for GSFC and TGLC, for which the volume of data on MAST is very large, we randomly selected 1% of the available GSFC and TGLC light curves per sector for comparison.

When comparing un-detrended light curves, we find that QLP and SPOC-TESS both tend to produce light curves with lower MAD than T16. We find that 28.8% of un-detrended T16 light curves have a lower MAD than the corresponding un-detrended SAP light curves from QLP, and 40.0% of un-detrended T16 light curves have a lower MAD than the un-detrended SAP light curves from SPOC-TESS. Here it is important to note that the Cycle 1 QLP light curves are not automatically corrected for contamination from neighboring stars. This can lead to an artificially low MAD in the magnitude light curves of faint stars blended with brighter stars. Such blending is a common occurrence given the  $21'' \text{ pixel}^{-1}$  plate scale of *TESS*. For T16 and SPOC-TESS the contamination flux is effectively subtracted from the light curves. When comparing the detrended light curves, we find that a majority of the T16 light curves have lower MAD than the corresponding QLP and SPOC-TESS light curves, with 78% of T16 detrended light curves having a lower MAD than the KSPSAP light curves from QLP, and 69.8% of T16 detrended light curves having a lower MAD than the PDCSAP light curves from QLP.

We find that 62.3% of the undetrended T16 light curves have lower MAD than their corresponding raw GSFC light curves, but this drops to 43.1% for the

detrended T16 light curves compared to the corrected GSFC light curves. We find that 79.5% and 73.7% of the undetrended T16 light curves have lower MAD than the TGLC aperture and psf photometry light curves, respectively, while 85.6% and 77.3% of the detrended T16 light curves have lower MAD than the respective calibrated TGLC light curves.

#### 4.3.2. Example Light Curve Comparison

*Transiting Planet Systems*—As a check of the light curve quality, we identified *TESS* Objects of Interest (TOIs) listed on the NASA Exoplanet Archive<sup>2</sup> for which we have produced a light curve. We used the VARTOOLS program to perform a Box Least Squares (BLS; Kovács et al. 2002) search for periodic transit signals in these light curves.

We searched the TFA-detrended light curves in all three available photometric apertures, treating the light curves from each sector, camera and CCD independently (i.e., we do not combine all light curves for a given target, but instead search the individual single sector light curves). In each case we search for periods between 0.2 days and 30 days, scanning 100,000 frequencies with 1000 phase bins per frequency. At each frequency we search a range of transit durations from half the expected duration for a zero-impact-parameter transiting planet on a circular orbit around a solar-density star,

<sup>2</sup> as of the date 2023 Jan 25; note that TOIs identified after this date are largely longer period candidates that have no, or few, transits in Cycle I, so we chose not update the analysis to include those objects.

to twice the expected duration for such a system. We identify the top five peaks in the periodogram for each run of BLS, fitting a trapezoid transit model at each identified peak.

We consider the transit signal to be recovered for the purposes of this exercise if one of the identified periods from at least one of the BLS runs for a given target has a period that is within 1% of the listed period, or an integer harmonic of the listed period (we consider the second through tenth harmonics). We note that because we are not combining the light curves from multiple sectors, cameras or CCDs, and we are not optimizing the BLS search on a star-by-star basis, we do not expect this search to recover all of the TOIs that might be recoverable within our data. We also note that many of the TOIs were identified based on *TESS* observations obtained after Cycle 1, so we do not expect to recover these signals within the light curves presented here. Based on the above selection method, we recover 2639 out of the 2971 TOIs for which we have produced a light curve. We conclude that our T16 light curves are of sufficient quality to recover the large majority of known transiting planet signals from *TESS*, even when running a non-optimized, single-sector search.

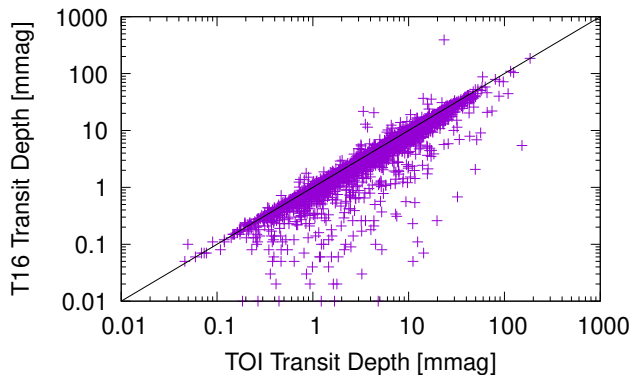


**Figure 14.** Comparison between the transit depth measured from a non-optimized BLS analysis of the TFA-detrended T16 light curves to the listed TOI transit depth for known TOIs for which we have produced a light curve. We only show this comparison for those objects for which the BLS transit ephemeris is consistent with the reported TOI ephemeris. The solid line shows equal transit depths.

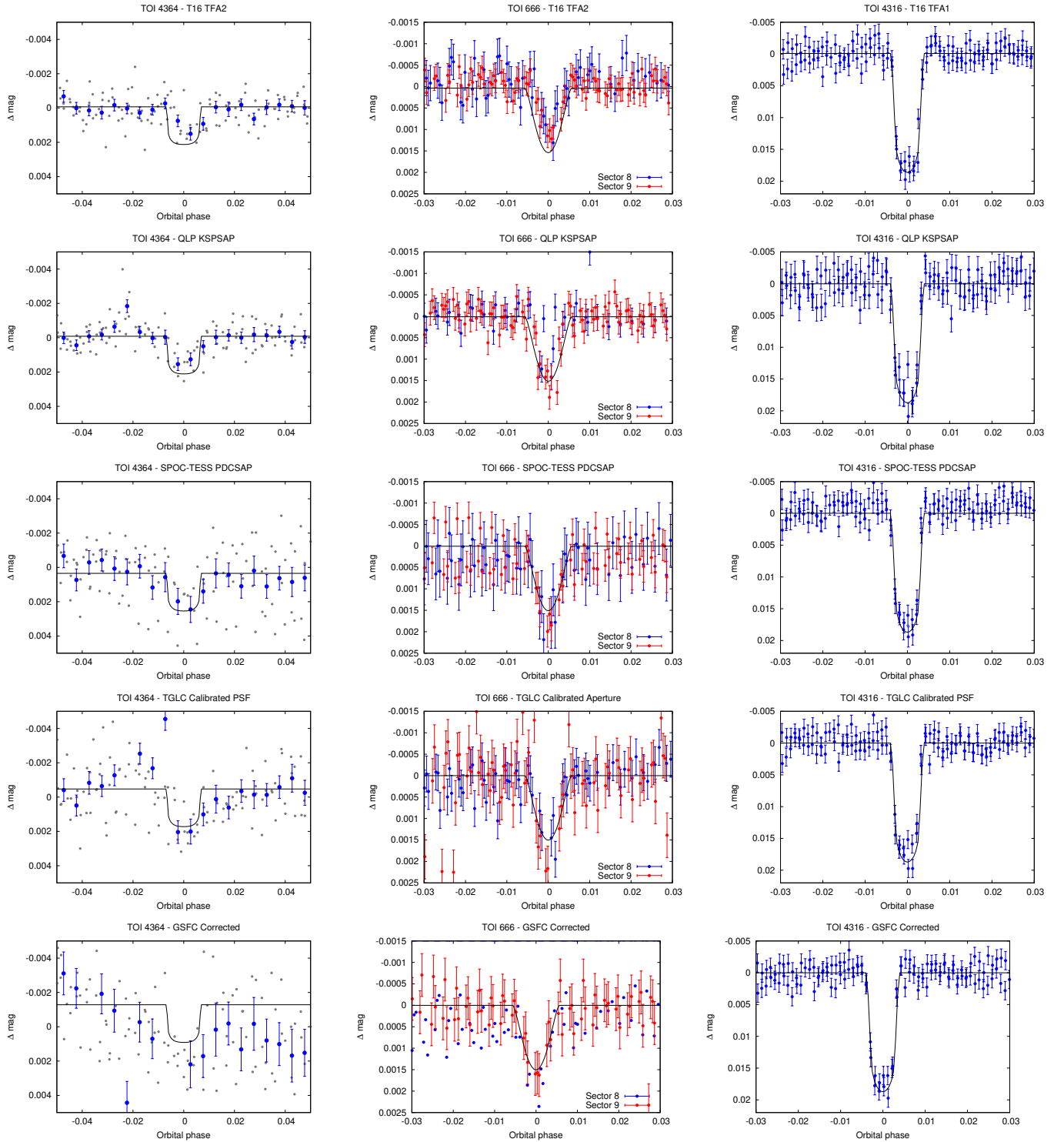
Figure 14 compares the transit depth from the TFA-detrended T16 light curves to the reported TOI transit depth. For simplicity the T16 transit depth is measured by performing a BLS transit search on each light curve at a period fixed to the reported TOI period, and we show only those systems for which the transit epoch recovered in the T16 light curve is consistent with the

reported TOI ephemeris. We find that the median ratio of the T16 transit depth to the reported TOI transit depth is 91%. The modest reduction in depth may be due to over-filtering by SEPD+TFA (these are being run without simultaneously fitting for any astrophysical variability signal), the simple BLS search finding a slightly longer transit duration or slightly offset transit epoch compared to the TOI values, and/or the use of a box-shape transit model rather than the limb-darkened model. We conclude that while there may be a slight distortion and damping of transit-like variable signals in our TFA-detrended light curves, overall the image subtraction light curves have variability amplitudes for transit systems that are in line with expectations.

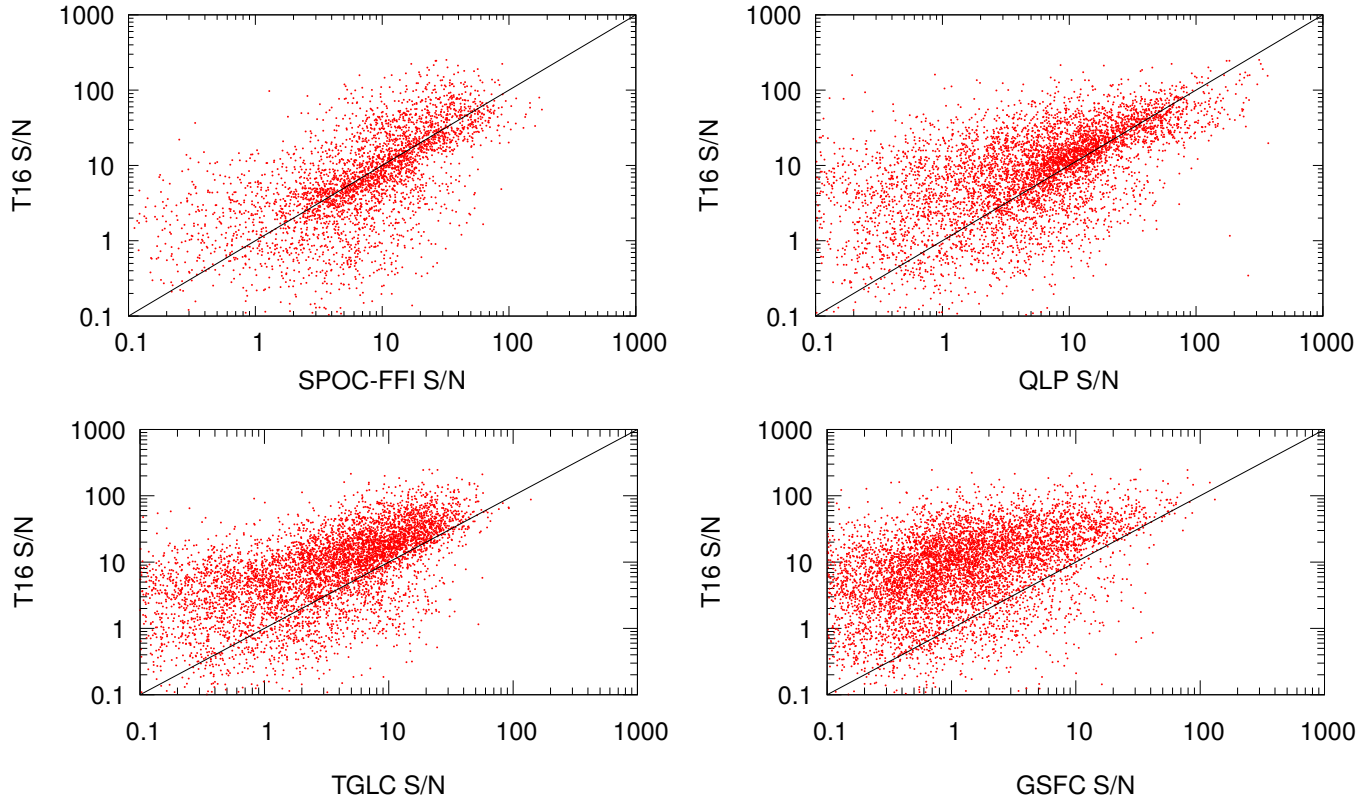
There are a number of cases where the T16 transit depth is significantly lower than the listed TOI value. We find 79 cases (corresponding to 2.5% of the sample) where the T16 depth is less than 10% of the TOI depth (counting only examples where there is at least one point in transit in the T16 light curve). There does not appear to be a single, simple explanation of these. The TOIs with low T16 transit depths do not have systematically fewer points in transit, systematically longer periods, or systematically different transit durations, or stellar apparent magnitudes than TOIs where the T16 transit depths match well to the TOI values. They also do not appear to be clustered in any particular region of the sky. We do find that 25% of the objects with exceptionally low T16 transit depths have been set aside as false positives or marked as likely eclipsing binaries or blended eclipsing binaries, which is higher than the 15% of the general sample of TOIs. One case (TOI 2556.01) has exceptionally strong TTVs that smear out the transits when folded at fixed period. In some cases the estimated reference flux based on applying our transformations to the Gaia DR2 photometry appears to be too high, yielding a transit depth that is too low in the image subtraction light curves.

Figure 15 compares the QLP, SPOC-FFI, TGLC, GSFC-ELEANOR-LITE, and T16 light curves for three representative TOIs (TOI 4364, TOI 666 and TOI 4316) for which light curves are available from all three projects. In all cases we show the phase-folded detrended light curves available on MAST from each project, and over-plot the same Mandel & Agol (2002) transit model evaluated for the fixed planetary system parameters taken from the ExoFOP-TESS webpage<sup>3</sup>. The three systems selected for display have transit S/N in the T16 light curves that is near the 10th, median

<sup>3</sup> <https://exofop.ipac.caltech.edu/tess/index.php>



**Figure 15.** Phase-folded detrended light curves from the T16 project (*top row*), QLP project (*second row*), SPOC-FFI project (*third row*), TGLC project (*fourth row*), and GSFC-ELEANOR-LITE project (*bottom row*) for three representative TOIs: TOI 4364 (*left column*), TOI 666 (*middle column*) and TOI 4316 (*right column*). For TOI 4364 we show the individual light curve observations as gray circles, while blue circles show the phase-binned values. For TOI 666 individual observations from Sectors 8 and 9 are shown using blue and red circles, respectively. For TOI 4316 we show only the individual observations using blue circles. For all three systems we overplot a [Mandel & Agol \(2002\)](#) transit model calculated using planetary system parameters taken from the ExoFOP-TESS website. For the T16 light curves the photometric aperture displayed is indicated above each panel. We show the calibrated aperture photometry TGLC light curve for TOI 666 and the calibrated PSF photometry TGLC light curves for the other two TOIs.



**Figure 16.** Comparison between  $S/N_{\text{pink}}$  measured from the T16 TFA-detrended light curves for known TOIs to  $S/N_{\text{pink}}$  measured from the SPOC-FFI light curves (*top left*), the QLP light curves (*top right*), the TGLC light curve (*bottom left*), and the GSFC-ELEANOR-LITE light curves (*bottom right*), for the same objects. The solid line shows where the two measures are equal. We find that  $S/N_{\text{pink}}$  is higher in the T16 light curves for 44.9%, 62.8%, 76.6% and 85.5% of TOIs compared to the SPOC, QLP, TGLC and GSFC-ELEANOR-LITE light curves, respectively.

and 90th percentile among all known TOIs with transits recoverable in the T16 light curves (Section 4.3.2.0). An extended figure set showing the T16 phase-folded light curves for all of the TOIs investigated is available at <https://doi.org/10.5281/zenodo.14278698>.

Figure 16 compares the  $S/N_{\text{pink}}$  measured from the T16 light curves for the TOIs to this same quantity measured from the SPOC, QLP, TGLC and GSFC light curves. Here  $S/N_{\text{pink}}$  is the signal-to-pink-noise ratio calculated by the `-BLSFixPerDurTc` command in `VARTOOLS`, and is defined in Hartman & Bakos (2016). We find that for 44.9% of cases, the T16  $S/N_{\text{pink}}$  is greater than the SPOC-FFI  $S/N_{\text{pink}}$ , for 62.8% of cases it is greater than the QLP  $S/N_{\text{pink}}$ , for 85.5% of cases it is greater than the corrected GSFC  $S/N_{\text{pink}}$ , and for 76.5% of cases it is greater than the calibrated PSF-photometry TGLC  $S/N_{\text{pink}}$ . We conclude that while the SPOC-FFI light curves may be somewhat better for transit recovery than the TFA-detrended T16 light curves, the T16 light curves are generally better for this purpose than the QLP, TGLC, or GSFC light curves. A significant

advantage of T16 over either SPOC-FFI or QLP is that fainter targets with  $T > 13.5$  mag are included in the T16 light curve release.

*Pulsating Variable Stars*—To evaluate the performance of the T16 reduction process on longer period variable sources, we inspected light curves for large amplitude Cepheid variable stars from the OGLE survey (Udalski et al. 2015, 2018; Soszyński et al. 2020). These stars are restricted to the Galactic plane. Figure 17 compares the T16 light curves for three representative Cepheids chosen to span a range of periods to the QLP light curves. Here we compare the un-detrended light curves from both projects, as both projects implement a detrending process that would distort large amplitude, longer period variable stars, such as these. We find that the T16 light curves, which include an effective ensemble magnitude correction through the image subtraction process, perform much better than the QLP SAP light curves for these stars. This is especially pronounced for the longer period variables, such as OGLE-GD-CEP-1859, with a period of 67.57 days, that shows a slow variation

in time in the T16 light curve over the course of Sector 11, but for which the variation is indistinguishable from other systematic artifacts in the QLP SAP light curve. We found much less overlap for variable stars like these with the SPOC-TESS project, due to the more restrictive selection of stars for which SPOC-TESS generated light curves.

We also use the OGLE Cepheid variables to assess the impact of our detrending methods on the amplitudes of variable stars. Fig. 18 compares the peak-to-peak amplitudes measured from the undetrended IRM light curves, and from the EPD- and TFA-detrended light curves for Cepheids from this catalog, as a function of period. The amplitudes are measured by fitting a 10-harmonic Fourier series to the T16 light curve, fixing the period to the value listed in the OGLE catalog. The results shown are for the smallest aperture photometry, and are similar to the results for the medium and largest apertures. We also show the ratios of the EPD to IRM and the TFA to IRM amplitudes as a function of period. For periods less than  $\sim 1$  day, the EPD amplitudes are generally consistent with the IRM amplitudes, while the TFA amplitudes show a slight reduction that is uncorrelated with the period. For periods longer than 1 day, the EPD and TFA amplitudes drop precipitously, and can be as low as  $\sim 1\%$  of the IRM amplitudes.

*Eclipsing Binary Stars*—We also inspected the light curves of eclipsing binary stars taken from the OGLE catalog of eclipsing binaries in the Galactic bulge (Soszyński et al. 2016). Again we find overlap for most of these objects only with the QLP light curves, and we show a comparison for three representative cases in Figure 19. As for Cepheids, we find that the undetrended T16 light curves provide more reliable measurements for these large amplitude variable stars than the undetrended QLP SAP light curves.

## 5. CONCLUSION

In this paper we have introduced the T16 project, which is producing image subtraction light curves for all stars with  $T < 16$  mag from the *TESS* Full-Frame Images. We have produced 83,717,159 light curves for 56,401,549 stars with  $T < 16$  mag from the *TESS* Cycle 1 Full-Frame Images, making use of the image subtraction carried out by the CDIPS project. Both raw, and detrended light curves are made available at <http://doi.org/10.17909/8nxx-tw70>. Additional

*TESS* Cycles are being processed, and the data will be released at this same location.

We compared our light curves to those from the QLP, SPOC-FFI, GSFC and TGLC projects. We find that the detrended T16 light curves have lower MAD for a majority of stars when compared to the detrended QLP, SPOC-FFI and TGLC light curves, whereas 43.1% of detrended T16 light curves have lower MAD than the detrended GSFC light curves. We find that 2639 out of 2971 TOIs have transit signals detectable in the Cycle 1 T16 light curves, and that the transit depth and S/N is generally comparable to that seen in the light curves from other projects.

We find that undetrended T16 light curves may be especially useful for studying large amplitude, and long time-duration variable stars. Such variations are often distorted in the light curves produced by other projects.

Finally, we note that a significant contribution of the T16 project is in simply providing light curves that are produced using a different method from other projects. The choice of which publicly available light curve to use will vary by the star and science goals of the investigation. We have found that all of the different projects produce the highest precision light curve available at least some of the time, and it is important to note that precision is not the only basis on which one might select a light curve. The more choices that are available for a given source, the more likely it is that there will be a high quality, scientifically useful light curve available.

The authors thank the anonymous referee for numerous helpful comments that improved the quality of the work. This project received funding from the NASA Astrophysics Data Analysis Program (ADAP) grant 80NSSC22K0409. We acknowledge the use of *TESS* High Level Science Products (HLSP) produced by the Quick-Look Pipeline (QLP) at the *TESS* Science Office at MIT, which are publicly available from the Mikulski Archive for Space Telescopes (MAST). Funding for the *TESS* mission is provided by NASA’s Science Mission directorate. We thank the data scientists at STScI for their assistance in making data from this project available on MAST.

*Facilities:* TESS

*Software:* FITSH (Pál 2012), VARTOOLS (Hartman & Bakos 2016), Astropy (Astropy Collaboration et al. 2013, 2018, 2022), Pandas (McKinney et al. 2010)

## REFERENCES

- Alard, C., & Lupton, R. H. 1998, ApJ, 503, 325
- Astropy Collaboration, Robitaille, T. P., Tollerud, E. J., et al. 2013, A&A, 558, A33



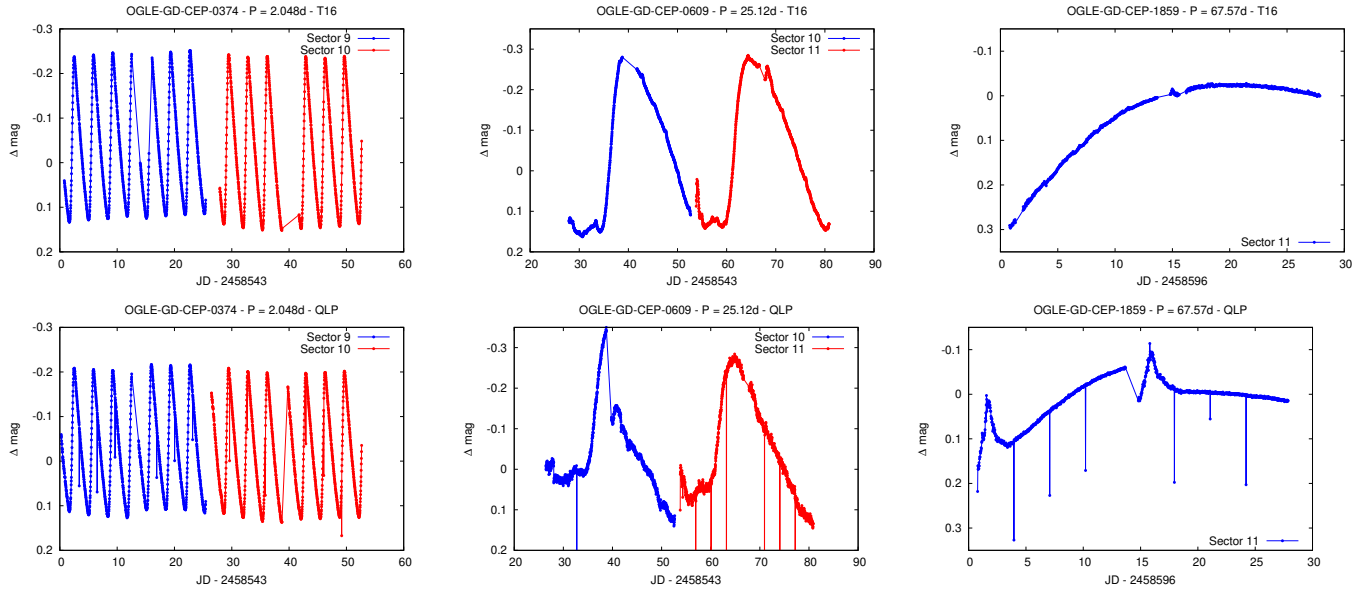


**Figure 17.** T16 (*top row*) and QLP (*bottom row*) light curves for three representative Cepheid variable stars taken from the OGLE catalog of variable stars in the Galactic plane (Udalski et al. 2015, 2018; Soszyński et al. 2020). The three stars shown here were selected to have a range of periods, as indicated in the title of each panel. For both the T16 and QLP light curves we show the un-detrended data (IRM magnitudes for T16, and SAP fluxes converted to magnitudes for QLP). SPOC-FFI light curves were not available for these three objects. While instrumental systematic variations are present in the T16 data, these artifacts are generally much less pronounced in the un-detrended T16 light curves than they are in the QLP SAP light curves.

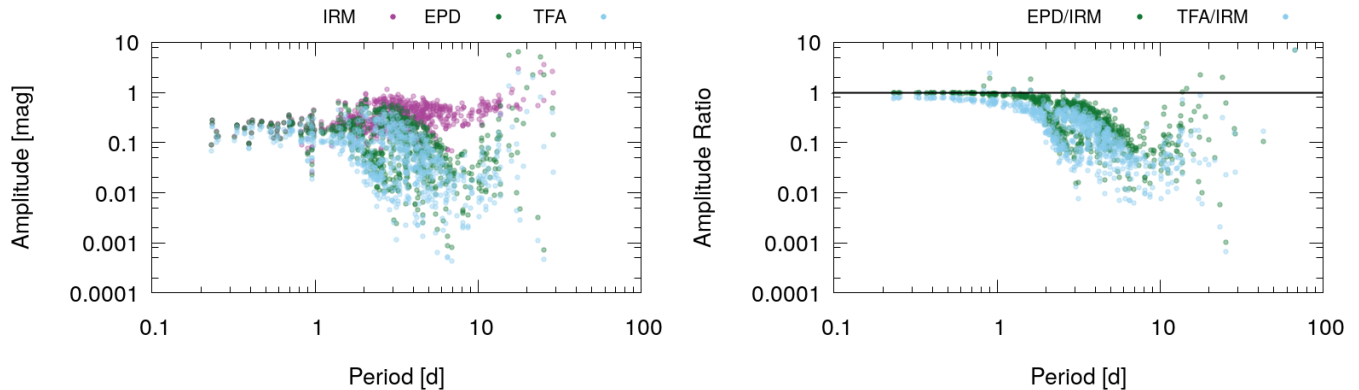


**Figure 18.** *Left:* Peak-to-peak amplitude vs. period for Cepheid variables from the OGLE catalog measured from the T16 undetrended IRM light curves, as well as the EPD- and TFA-detrended light curves. A few example light curves are shown in Fig. 17. *Right:* The ratio of the EPD to IRM and TFA to IRM amplitudes as a function of period for the same Cepheid variables. For periods greater than  $\sim 1$  day the EPD- and TFA-detrended light curves have significantly lower amplitudes than the undetrended IRM light curves, with the amplitude of the signal suppressed by as much as a factor of  $\sim 100$  and some cases.

Astropy Collaboration, Price-Whelan, A. M., Sipőcz, B. M., et al. 2018, *AJ*, 156, 123

Astropy Collaboration, Price-Whelan, A. M., Lim, P. L., et al. 2022, *ApJ*, 935, 167

Bouma, L. G., Hartman, J. D., Bhatti, W., Winn, J. N., & Bakos, G. Á. 2019, *ApJS*, 245, 13

Caldwell, D. A., Tenenbaum, P., Twicken, J. D., et al. 2020, *Research Notes of the American Astronomical Society*, 4, 201

Feinstein, A. D., Montet, B. T., Foreman-Mackey, D., et al. 2019, *PASP*, 131, 094502

Gaia Collaboration, Brown, A. G. A., Vallenari, A., et al. 2018, *A&A*, 616, A1

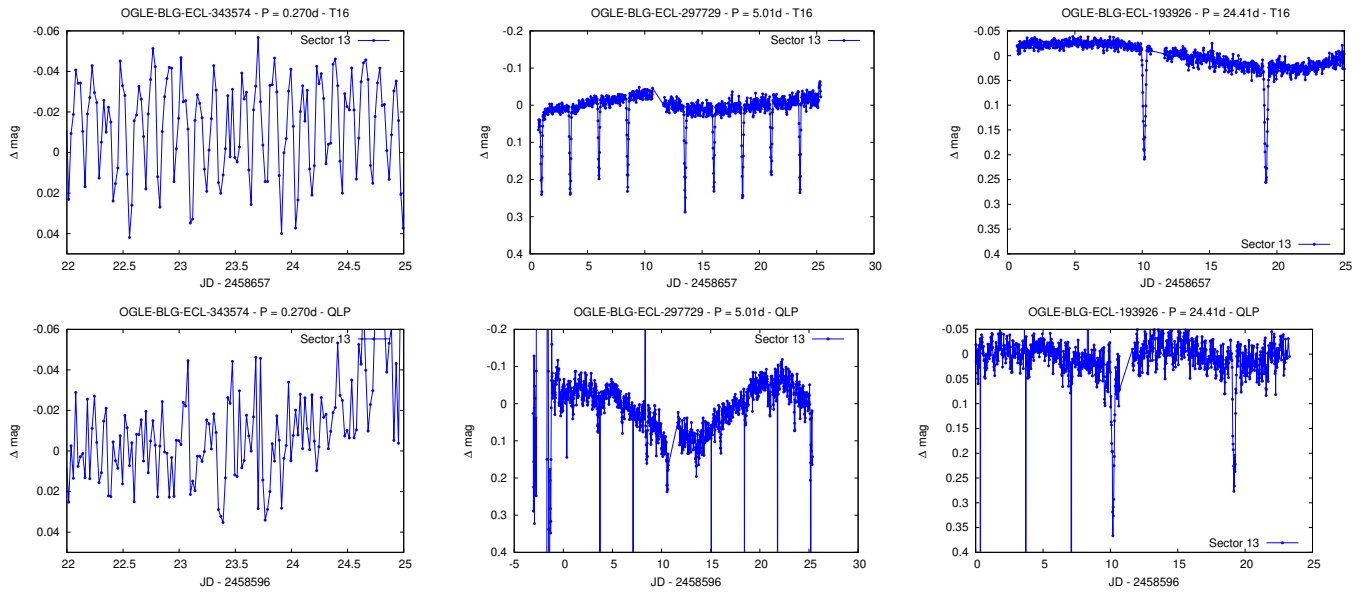


**Figure 19.** Similar to Fig. 17, here we compare the T16 (*top row*) and QLP (*bottom row*) light curves for three representative Eclipsing binary stars taken from the OGLE catalog of variable stars in the Galactic bulge (Soszyński et al. 2016). For OGLE-BLG-ECL-343574 we show only 3 days of data to make the individual eclipses visible. As for the Cepheids, we find that the un-detrended T16 light curves have much lower instrumental systematic artifacts compared to the un-detrended QLP light curves for these deep eclipsing binary stars in the highly crowded Galactic bulge.

Giorgini, JD and JPL Solar System Dynamics Group. 2023, NASA/JPL Horizons On-Line Ephemeris System, vVersion: 2023-07-24, NASA/JPL.

<https://ssd.jpl.nasa.gov/horizons/>

Han, T., & Brandt, T. D. 2023, AJ, 165, 71

Hartman, J. D., & Bakos, G. Á. 2016, Astronomy and Computing, 17, 1

Huang, C. X., Vanderburg, A., Pál, A., et al. 2020a, Research Notes of the American Astronomical Society, 4, 204

—. 2020b, Research Notes of the American Astronomical Society, 4, 206

Ivezić, Ž., Connolly, A. J., VanderPlas, J. T., & Gray, A. 2014, Statistics, Data Mining, and Machine Learning in Astronomy: A Practical Python Guide for the Analysis of Survey Data, doi:10.1515/9781400848911

Jenkins, J. M., Twicken, J. D., McCauliff, S., et al. 2016, in Society of Photo-Optical Instrumentation Engineers (SPIE) Conference Series, Vol. 9913, Software and Cyberinfrastructure for Astronomy IV, ed. G. Chiozzi & J. C. Guzman, 99133E

Kovács, G., Bakos, G., & Noyes, R. W. 2005, MNRAS, 356, 557

Kovács, G., Zucker, S., & Mazeh, T. 2002, A&A, 391, 369

Kunimoto, M., Tey, E., Fong, W., et al. 2022, Research Notes of the American Astronomical Society, 6, 236

Kunimoto, M., Huang, C., Tey, E., et al. 2021, Research Notes of the American Astronomical Society, 5, 234

Mandel, K., & Agol, E. 2002, ApJL, 580, L171

McKinney, W., et al. 2010, in Proceedings of the 9th Python in Science Conference, Vol. 445, Austin, TX, 51–56

Montalto, M. 2023, MNRAS, 518, L31

Montalto, M., Borsato, L., Granata, V., et al. 2020, MNRAS, 498, 1726

Nardiello, D. 2020, MNRAS, 498, 5972

Nardiello, D., Borsato, L., Piotto, G., et al. 2019, MNRAS, 490, 3806

Nardiello, D., Piotto, G., Deleuil, M., et al. 2020, MNRAS, 495, 4924

Nardiello, D., Deleuil, M., Mantovan, G., et al. 2021, MNRAS, 505, 3767

Pál, A. 2012, MNRAS, 421, 1825

Powell, B. P., Kruse, E., Montet, B. T., et al. 2022, Research Notes of the American Astronomical Society, 6, 111

Ricker, G. R., Winn, J. N., Vanderspek, R., et al. 2015, Journal of Astronomical Telescopes, Instruments, and Systems, 1, 014003

Soszyński, I., Pawlak, M., Pietrukowicz, P., et al. 2016, AcA, 66, 405

Soszyński, I., Udalski, A., Szymański, M. K., et al. 2020, AcA, 70, 101

Stassun, K. G., Oelkers, R. J., Paegert, M., et al. 2019, AJ, 158, 138

Udalski, A., Szymański, M. K., & Szymański, G. 2015,  
AcA, 65, 1

Udalski, A., Soszyński, I., Pietrukowicz, P., et al. 2018,  
AcA, 68, 315